A Simplified Scheme for Obtaining Precipitation and Vertical Hydrometeor Profiles from Passive Microwave Sensors

Christian Kummerow, William S. Olson, and Louis Giglio

Abstract—**This paper presents a computationally simple technique for retrieving the precipitation and vertical hydrometeor profiles from downward viewing radiometers. The technique is computationally much less expensive than previous profiling schemes and has been designed specifically to allow for tractability of assumptions. In this paper, the emphasis is placed upon passive microwave applications, but the combination of passive with active microwave sensors, infrared sensors, or other *a priori* information can be adapted easily to the framework described here. The technique is based upon a Bayesian approach. Here, we use many realizations of the Goddard Cumulus Ensemble model to establish a prior probpability density function of rainfall profiles. Detailed three-dimensional radiative transfer calculations are used to determine the upwelling brightness temperatures from the cloud model to establish the similarity of radiative signatures and thus the probability that a given profile is actually observed. In this study, we show that good results may be obtained by weighting profiles from the prior probability density function according to their deviation from the observed brightness temperatures. Examples of the retrieval results are shown for oceanic as well as land situations. Microwave data from the Advanced Microwave Precipitation Radiometer (AMPR) instrument are used to illustrate the retrieval structure results for high-resolution data while SSM/I is used to illustrate satellite applications. Simulations are performed to compare the expected retrieval performance of the SSM/I instrument with that of the upcoming TMI instrument aboard the Tropical Rainfall Measuring Mission (TRMM) to be launched in August 1997. These simulations show that correlations of ~0.77 may be obtained for 10-km retrievals of the integrated liquid water content based upon SSM/I channels. This correlation increases to ~0.90 for the same retrievals using the TMI channels and resolution. Due to the lack of quantitative validation data, hydrometeor profiles cannot be compared directly but are instead converted to an equivalent reflectivity structure and compared to existing radar observations where possible.**

I. Introduction

MICROWAVE remote sensing of clouds and precipitation has shown great promise because of the direct interaction between hydrometeors and the radiation field. Unlike infrared measurements which are sensitive only to the uppermost layer of clouds, microwave radiation has the ability to penetrate the clouds and offer insight into the structure of the rainfall itself. Passive microwave sensors have flown on a number of spaceborne platforms. These include the Nimbus 5 and Nimbus 6 spacecraft (launched in 1972 and 1976, respectively) with the Electronically Scanned Microwave Radiometer (ESMR). The ESMR was a single-channel 19.35-GHz instrument scanning cross track between $\pm 45^{\circ}$ of nadir. In 1978, the Scanning Multichannel Microwave Radiometer (SMMR) was launched aboard Seasat and Nimbus 7. It measured brightness temperatures at five frequencies (6.6, 10.7, 18.0, 21.3, and 37.0 GHz) for both horizontal and vertical polarizations. Finally, in 1987, the first Special Sensor Microwave/Imager was launched on the Defense Meteorological Satellite Program (DMSP) F-8 satellite. Since then, three additional SSM/I instruments have been launched. DMSP F-10 was launched in December 1990. DMSP F-11 was launched in November 1991 to replace the ailing F-8, and DMSP-12 was launched in August 1994 although its SSM/I sensor is currently spun down. The SSM/I is a seven-channel (19.35 H&V, 21.235 V, 37.0 H&V, and 85.5 H&V GHz), conically scanning radiometer that has proved itself stable and well calibrated. In the near future, microwave data will be provided by the Tropical Rainfall Measuring Mission (TRMM) satellite scheduled to launch in August 1997 (see [1]). TRMM will carry the first precipitation radar which is a cross-track scanning 13.8-GHz instrument as well as the TRMM Microwave Imager (TMI) which is a copy of the SSM/I except that channels at 10.7 GHz (vertical and horizontal polarizations) are added and the water vapor channel is moved from 22.235 to 21.3 GHz to avoid saturation in the tropics.

The oceans radiate microwave energy equivalent to εT_s where ε is the surface emissivity (~0.5 for typical microwave frequencies). For passive microwave observations, the ocean therefore appears uniformly cold. Raindrops in the atmosphere act to absorb and re-emit radiation at their own thermodynamic temperature thus increasing the observed brightness temperatures. Algorithms which make use of this relationship are commonly referred to as "emission"-based algorithms. Perhaps the best known example of such an algorithm is due to [2]. Longer wavelengths tend to saturate at higher rainfall rates and are less sensitive to the effects of ice scattering. That makes these wavelengths (19 and 37 GHz) better suited for emission type algorithms. Emission algorithms, however, cannot work

Manuscript received June 29, 1995; accepted March 1, 1996. This work was supported by Dr. R. Kakar of NASA Headquarters, as part of the TRMM algorithm development effort.

C. Kummerow is with Goddard Space Flight Center/NASA, Greenbelt, MD 20771 USA.

W. S. Olson is with Caelum Research Corporation, Silver Spring, MD 20907 USA.

L. Giglio is with Science Systems and Applications, Inc., Lanham, MD 20706 USA.

Publisher Item Identifier S 0196-2892(96)05055-3.

over land where high surface emissivities (~0.9) obscure the emission signal. They are also plagued by resolution problems which cause inversion algorithms that do not consider the inhomogeneity of rainfall to seriously underestimate the rainfall.

As microwave frequencies increase, so does the amount of scattering due to ice particles commonly found in raining clouds. This scattering acts to reflect upwelling radiation back to the surface, lowering the observed brightness temperatures. While all frequencies display some amount of scattering, the behavior is most evident in the 85-GHz channel of the SSM/I where brightness temperature depressions of as much as 150 K can be observed over convective updrafts. Algorithms which make use of this relationship are generally referred to as "scattering" algorithms. Examples of this type of algorithm can be found in [3], [4], or [5]. Scattering algorithms work over both land and water and are able to take advantage of the better spatial resolution offered by the high frequency channels. While this has made the algorithms very popular, scattering algorithms must infer the precipitation based upon a measure related to the ice content of the cloud. This makes scattering algorithms more susceptible to regional and temporal biases than the more direct estimates made by emission methods.

In addition to emission and scattering algorithms, there are also a number of multichannel regression algorithms. Examples of these may be found in [6], or the SSM/I Calibration/Validation algorithm described by [7]. The algorithms are based upon theoretical radiative transfer computations to derive regression statistics. In so doing, however, these algorithms become sensitive to the assumed vertical structure of rain systems. Unless the ratios of cloud water, rain water, and ice in the cloud systems are assumed correctly, these schemes are susceptible to the same uncertainties found in pure scattering algorithms. To avoid some of these problems, [8] have developed alternative approaches in which emission signatures are used to determine rainfall while scattering signatures are used to help define the nature of the precipitation. To overcome the inhomogeneous rainfall problem, [9] has developed a technique that employs normalized polarization and scattering indices.

As can be seen from the diversity of approaches, the theoretically straightforward relationship between raindrops and radiation in the microwave region is generally complicated by a myriad of related problems such as the nature of the surface, the amount and distribution of nonprecipitating cloud water, the phase of the hydrometeors, the horizontal as well as vertical distribution of hydrometeors, and the uncertainties in the radiative transfer models themselves. A final class of algorithms which includes the one described in this paper consists of inversions schemes which seek to overcome some of these problems by simultaneously retrieving the entire vertical structure of the precipitation. This is made possible by the fact that response functions for different channels peak at different depths within the raining column. These algorithms, sometimes referred to as profiling algorithms, have in common that they vary an assumed rain structure in order to minimize the differences between observed and modeled radiances. Examples of these algorithms can be found in [10]–[13]. The major drawback of these algorithms to date has been the fact that they all require radiative transfer computations within an iterative minimization scheme. This has made these algorithms extremely expensive to implement in a routine fashion. Research motivated by the TRMM has led to the present work which borrows ideas from much of the previous work to build a profiling algorithm (referred to as the Goddard Profiling Alforithm, GPROF) which is intuitively simple, computationally much less intensive than its predecessors and expandable to include not only passive microwave, but radar or infrared observations as well.

II. Retrieval Method

Radiative transfer calculations can be used to determine a brightness temperature vector, $\mathbf{TB}$, given a vertical distribution of hydrometeors represented by $\mathbf{R}$. An inversion procedure, however, is needed to find the hydrometeor profile, $\mathbf{R}$, given a vector $\mathbf{TB}$. The present retrieval method has its foundation in Bayes theorem. In Bayes's formulation, the probability of a particular profile $\mathbf{R}$, given $\mathbf{TB}$ can be written as

$$\Pr(\mathbf{R}|\mathbf{TB}) = \Pr(\mathbf{R}) \times \Pr(\mathbf{TB}|\mathbf{R}) \tag{1}$$

where $\Pr(\mathbf{R})$ is the probability with which a certain profile $\mathbf{R}$ will be observed and $\Pr(\mathbf{TB}|\mathbf{R})$ is the probability of observing the brightness temperature vector, $\mathbf{TB}$, given a particular rain profile $\mathbf{R}$. The first term on the right hand side of (1) is derived using the Goddard Cumulus Ensemble model (GCE) which is a cloud microphysical model developed mainly by [14]. While the model itself is only reviewed briefly, those aspects of the model which are important to the current discussion are described in detail in Section II-A. To obtain the second term on the right hand side of (1), we first discuss possible radiative transfer schemes, and then the convolution of brightness temperatures to match either aircraft or satellite fields of views. Together, the radiative transfer and the convolution scheme comprise the forward modeling portion of the retrieval algorithm which is covered in Section II-B. The inversion scheme (Section II-C) follows the description of the forward problem.

A. The Goddard Cumulus Ensemble Model

During the past two decades, convective scale models have advanced sufficiently to study the dynamic and microphysical processes associated with mesoscale convective systems. The basic feature of these models are that they are nonhydrostatic and include a good representation of microphysical processes. The current model's framework is based upon the original cloud ensemble model developed by Soong and Ogura [15]–[17]. However, many significant improvements have been made in the past decade at Goddard. Chief among these have been the addition of ice-microphysical processes as well as solar/infrared radiative transfer processes. The model was officially renamed the Goddard Cumulus Ensemble model in 1989.

The cloud microphysics include a parameterized Kessler type two-category liquid water scheme (cloud water and

rain), and parameterized [18] three-category ice phase schemes (cloud ice, snow, and hail/graupel). The shapes of liquid and ice are assumed to be spherical. The distributions of rain, snow, and graupel (or hail) are taken to be inverse exponential with respect to the diameter (D) such that

$$N(D) = N_0 \exp(-\lambda D) \tag{2}$$

where $N(D)$ is the number of drops of diameter between D and $D + dD$ per unit volume, N_0 is the intercept parameter and λ is the slope of the distribution given by

$$\lambda = \left(\frac{\pi \rho_x N_0}{\rho q_x}\right)^{0.25}. \tag{3}$$

The typical intercept parameters used in the GCE model for rain, snow, and graupel are 0.08, 0.04, and 0.04 cm^{-4}, respectively. The density of rain, snow, and graupel are 1, 0.1, and 0.4 $g \cdot cm^{-3}$, respectively. The cloud ice is monodisperse with its diameter of 2×10^{-3} cm and a density of 0.917 $g \cdot cm^{-3}$.

Short-wave (solar) and long-wave (infrared) radiation parameterizations have recently been included in the GCE model. In the near infrared region, the computation of absorption of solar radiation by water vapor follows that of [19] and [20]. In the short-wave region, the computation of the absorption by ozone follows [21]. The absorption of O_2 and CO_2 near the visible and near-IR regions is included using the parameterization of [22]. In cloudy atmospheres, the four-stream discrete ordinate method of [23] is used to compute transmittance and reflectance of cloudy layers. The long wave scheme takes into account the effects of both gaseous and hydrometeor absorption. For gaseous absorption, the effects of water vapor, carbon dioxide, and ozone are computed.

A stretched vertical coordinate (height increments from 220 to 1050 m) with 31 grid points is used in order to maximize the resolution of the lowest levels. The model top can be 20–25 km. In the three-dimensional model, current computers limit simulations to about 218×54 grid points (using 1- or 1.5-km resolution) in the horizontal and 32 grid points (up to a depth of 22 km) in the vertical. For line-type convection, an open-type lateral boundary condition is used along the x-axis in the direction perpendicular to the line convection and a periodic lateral boundary condition is applied along the y-axis. However, open lateral boundary conditions can also be used in the y-axis for simulating isolated storms.

B. The Forward Model

1) Radiative Transfer Calculations: The observed microwave radiances at the top of the atmosphere originate partly at the earth's surface and partly from atmospheric constituents. The contribution from the earth's surface depends primarily upon the nature of the surface (i.e., water or land) and on the temperature of that surface. Atmospheric constituents such as oxygen, water vapor, and cloud water act to absorb and emit upwelling radiation. Large, precipitation drops further act to scatter upwelling radiation. Because of the varied, and often complex nature of each of these components, it is necessary to first understand the radiative properties of each of these components before attempting to understand the propagation of radiation through the medium.

The emissivity, ε, of a surface is determined by the frequency, incidence angle and polarization of the radiation, and by the complex index of refraction of the surface as described by the Fresnel relations [24]. Over oceans, the refractive index is a function of the temperature, the salinity, and the surface roughness induced by wind driven waves. While the effects of temperature and salinity are well understood, the effect of surface roughening is much more uncertain. In this study, the model of [25] is used to compute the ocean emissivity as a function of near-surface wind speed. While this model provides a satisfactory first order correction to account for wind induced roughening, it is recognized that this is an area of ongoing research that requires attention. Over land, the surface emissivity is generally assumed to be 0.9 for moderately dry, bare soil. This value is affected primarily by soil roughness, soil moisture and vegetation cover. Since none of these parameters are generally known, there seems little hope at this time to refine the land emissivity estimates even if the individual effects of the parameters affecting land emissivity were better understood.

Among atmospheric absorbers of microwave radiation, water vapor, molecular oxygen and cloud water, need be considered. Water vapor has a weak pressure broadened absorption line at 22.235 GHz and a strong line at 183 GHz. The 22.235 GHz line is of special significance in this study since it corresponds to a frequency measured by the SSM/I. Oxygen displays a strong complex of lines at 60 GHz as well as a single transition line at 118 GHz. The atmosphere is relatively clear in the window regions between these absorption lines. In this study, both the water vapor absorption as well as the oxygen absorption are calculated from [26]. Nonprecipitating cloud particles are of the order of 100 μm or less in diameter. This dimension is much smaller than typical wavelengths under consideration (3.5 mm–3 cm), thus permitting the use of the Rayleigh approximation. The absorption coefficient in this case depends only upon the dielectric constant of the liquid and upon the third power of the diameter of the cloud droplets. Thus, the absorption of the cloud water is simply proportional to the total mass of cloud water and is independent of the droplet size distribution. Scattering is negligible in this limit.

As cloud drops coalesce into raindrops, their dimensions can get comparable to microwave wavelengths and the Rayleigh approximation becomes invalid. If particles are assumed spherical, Mie theory may be employed. For shapes other than spheres, solutions like the Extended Boundary Condition Method [27], or the discrete dipole approximation [28] must be employed. The difficulties introduced by any these methods are three-fold. The first is due to the fact that scattering parameters exhibit resonance features that effectively increase the scattering efficiency beyond the third power of the drop diameter. This causes the volume scattering characteristics to depend upon the drop size distribution. The second difficulty introduced by the larger size parameters is the fact that scattering becomes important. In the case of 85 GHz, ice scattering from precipitation size hydrometeors becomes the dominant characteristic. Finally, it must be mentioned that

computationally these codes are all far more intensive than the closed form expression of the Rayleigh approximation. Mie scattering calculations can be very time consuming, while nonspherical codes are generally prohibitive for anything but a limited number of cases. For all practical purposes, these calculations can only be used through lookup tables containing implicit assumptions of drop size distributions and ice density in the case of frozen hydrometeors.

Once the radiative properties of the surface and atmosphere are known, a number of techniques may be used to compute the upwelling radiances. Two techniques have been considered in this study. The first technique, a one-dimensional Eddington approximation, has been used extensively during the development of the inversion technique. The details of the Eddington approximation, as well as its accuracy (1–2 K for the present application) are summarized by [29]. While the accuracy of the approximation is fully adequate, the one-dimensional treatment of the inherently three-dimensional problem causes errors and biases which can become significant in areas of large hydrometeor gradients. The second, more complete treatment of the radiative transfer problem is done using a recently developed backward Monte Carlo scheme. In this scheme the photons are started at the point at which the brightness temperature, Tb, is to be computed, in the direction opposite to that in which they would physically propagate inside the medium. Each photon is then traced backward through the medium following probabilistic interaction laws until the photon is absorbed. Absorbed photons are treated as being emitted at the point of absorption x with Tb equal to the physical temperature of the medium at that point $T(x)$. While computationally not trivial, the backward Monte Carlo approach does make it possible to generate useful results on a mid-sized workstation. Details of the procedure can be found in [30].

Fig. 1 shows hydrometeor fields generated by the GCE model. A more detailed representation of the integrated liquid and ice fields for the cross section at $x = 17$, is shown in the top panel of Fig. 2. The middle and bottom panels of Fig. 2 show the brightness temperatures generated from both the 1-D plane parallel Eddington as well as the 3-D Monte Carlo schemes for 19 and 85 GHz, respectively. The 1-D Eddington calculations are performed independently for each 1.5×1.5 km cloud model pixel in this calculation. At 19 GHz, the high-resolution plane parallel results can be seen to be slightly warmer than the Monte Carlo results throughout the region of significant water content. The difference in these regions of high absorption can be attributed to the fact that photons in the Monte Carlo are allowed to leak out of the regions of greatest absorption to nearby pixels. Near $y = 48$, this departure is further amplified by the large and rapidly changing ice content which acts to scatter the radiation further from the source. Although not very evident in this figure, the excess radiation is generally seen to emerge near the regions of high absorption. Large area differences or biases are generally quite small for absorption frequencies as shown in Table I. At 85 GHz, the biases are reversed due to the fact that scattering is the dominant radiative interaction. When the ice layer becomes optically thick, much of the radiation in the plane parallel solution is scattered back toward the surface. In the 3-D case, photons are free to move about in the horizontal dimension and thus more apt to find pockets of diminished scattering through which they can emerge. This phenomenon can cause plane parallel approximations to underestimate Tbs in significant regions of precipitating clouds and can produce nontrivial biases.

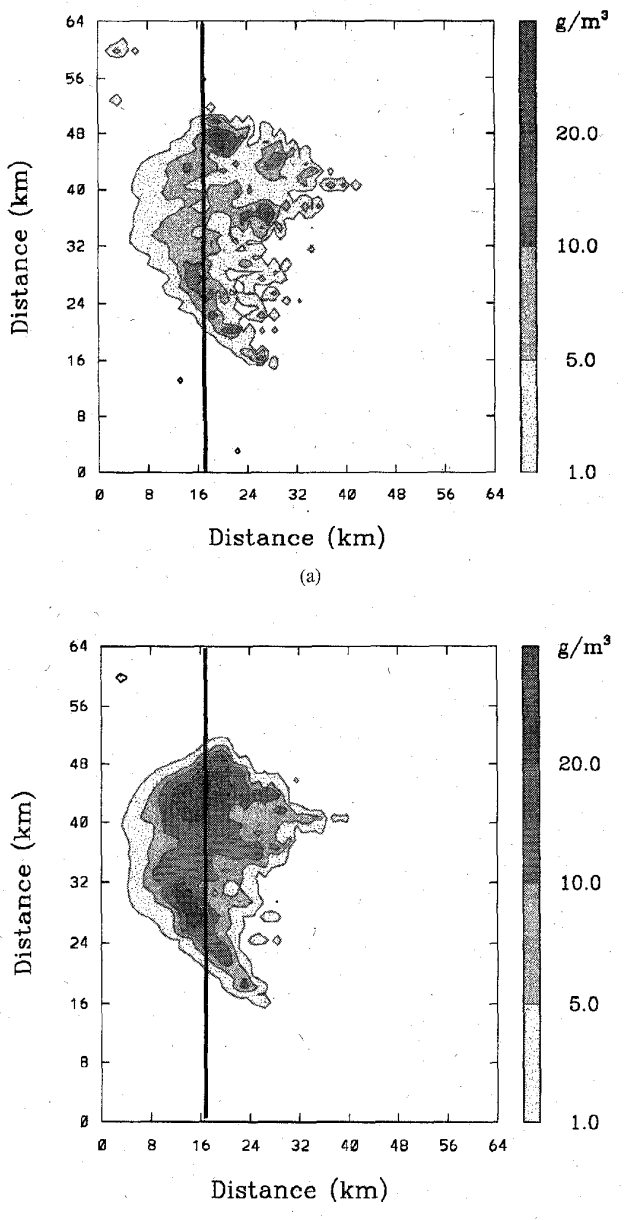

Fig. 1. (a) Integrated liquid water and (b) ice contents generated by the Goddard Cumulus Ensemble model "GATE" simulation.

While the 1-D independent pixel computations show occasional large departures from the true 3-D brightness temperatures, the most relevant quantities in satellite remote sensing are not the point by point differences presented above, but rather the differences and biases that might be observed at satellite footprint resolutions. The average brightness temper-

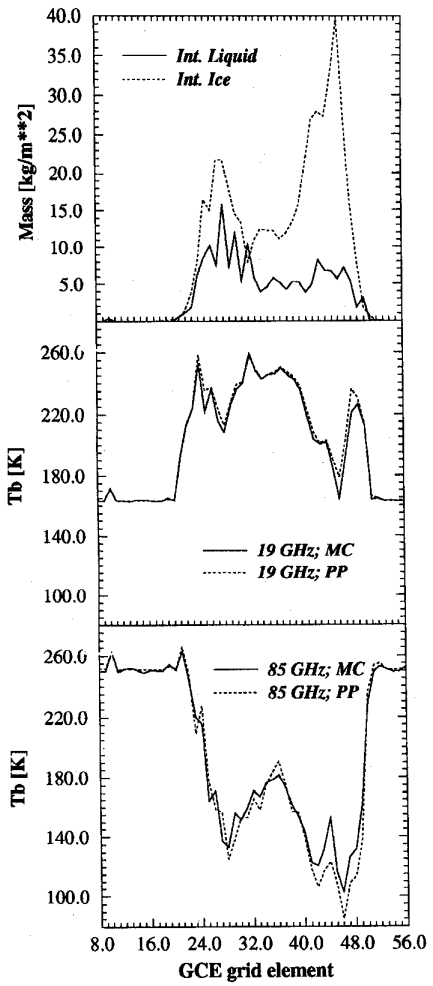

Fig. 2. Top panel: Integrated liquid and ice water content generated by the Goddard Cumulus Ensemble model along the $x = 17$ line shown in Fig. 1. Center and bottom panels: Comparison of brightness temperatures obtained from 1-D plane parallel and 3-D Monte Carlo calculations along the $x = 17$ line displayed in the top panel.

atures over 12 × 12 km areas corresponding to the highest sampling density of the SSM/I are used to illustrate the differences. Two comparisons are made in Table I. The first is the comparison between the Monte Carlo results and the 1-D independent pixel calculations described above. While the mean differences are generally small, it is possible to get significant departures over individual pixels as seen from the maximum difference entries. These pixels can make significant contributions to the total retrieved rainfall. The second comparison is made between the Monte Carlo results and 1-D averaged hydrometeor computations. In these 1-D computations, the hydrometeors are averaged first and plane parallel computations are then applied to the uniform hydrometeor field. These calculations are included to demonstrate the danger of treating individual satellite size footprints as homogeneous in the radiative transfer calculations. Unlike the plane parallel independent pixel calculations shown in Fig. 2, averaging the hydrometeors before performing the radiative transfer calculations introduces large errors and biases. It is

TABLE I
COMPARISON OF RADATIVE TRANSFER METHOD ON THE CALCULATED BRIGHTNESS TEMPERATURES FOR 12 × 12 km PIXELS. ONLY RAINING PIXELS ARE CONSIDERED

		10 GHz	19 GHz	37 GHz	85 GHz
Mean Diff.:	$PP_{Indep.\ Pixel}$ / MC	0.8K	1.2K	2.0K	2.7K
Max. Diff	$PP_{Indep.\ Pixel}$ / MC	2.7K	5.3K	6.4K	12.1K
Bias	$PP_{Indep.\ Pixel}$ – MC	–0.3K	+0.2K	+0.2K	+0.7K
Mean Diff.:	$PP_{Avg.\ Hydro}$ / MC	7.4K	14.6K	17.8K	14.2K
Max. Diff	$PP_{Avg.\ Hydro}$ / MC	26.1K	41.4K	50.9K	29.0K
Bias	$PP_{Avg.\ Hydro}$ – MC	+5.34K	+14.18K	+17.40K	–0.88K

this difference which causes the so called "footprint filling bias" present in most emission based (19 or 37 GHz) algorithms. By not accounting for the natural inhomogeneity of rainfall in the radiative transfer calculations, the brightness temperatures corresponding to average hydrometeor fields tend to be significantly warmer than the actual 3-D fields. This excessive warming of brightness temperatures in turn causes underestimates in the retrieved rainfall if the rainfall inhomogeneity effects are not corrected for.

2) Antenna Convolution: Once high-resolution brightness temperature fields have been calculated using either plane parallel or Monte Carlo methods, it is necessary to simulate the radiances as they would be measured from a downviewing microwave sensor. This is accomplished by convolving the brightness temperature field with the antenna gain function. For each channel, ν, the measured temperature $Tb(s_0)$ may be expressed as

$$Tb_\nu(s_0) = \int G_\nu(s_0, s)\, Tb_\nu(s)\, dA \tag{4}$$

where $G_\nu(s_0, s)$ is the antenna gain function for channel ν at position s relative to antenna boresight position, s_0, and $Tb_\nu(s)$ is the high-resolution brightness temperature calculated from the cloud model.

Sensitivity experiments using synthetic data show that the retrieval procedure is not very sensitive to the exact specification of the antenna gain function. A step function having the appropriate spatial resolution tended to perform almost the same as when the exact antenna gain function was employed in the retrieval. Thus, while it is more accurate to use the exact antenna gain function when it is known, using approximate gain functions does not appear to be a limiting factor in the retrieval at this time. In this study, all channels are convolved with an approximate antenna gain function. The effects of deconvolution schemes which increase the spatial resolution at the expense of some additional noise [31], [32] have not been examined.

C. Inversion Method

1) Theoretical Basis: In this development, the vector $\boldsymbol{x}$ is used to represent all of the physical quantities to be retrieved in the inversion method, and the vector $\boldsymbol{y}_0$ represents the set of available sensor observations. Following [33], it is assumed that the "best" estimate of $\boldsymbol{x}$, given the set of observations $\boldsymbol{y}_0$,

is the expected value

$$E(\boldsymbol{x}) = \iint \cdots \int \boldsymbol{x} \quad \text{pdf}\,(\boldsymbol{x})\, d\boldsymbol{x} \tag{5}$$

where the probability density function $\text{pdf}\,(\boldsymbol{x})$ is proportional to the conditional probability that $\boldsymbol{x}$ represents the true earth/atmosphere state, $\boldsymbol{x}_{\text{true}}$ given that $\boldsymbol{y}$ is equal to the observed $\boldsymbol{y}_0$:

$$\text{pdf}\,(\boldsymbol{x}) \propto P(\boldsymbol{x} = \boldsymbol{x}_{\text{true}} | \boldsymbol{y} = \boldsymbol{y}_0). \tag{6}$$

The expected value $E(\boldsymbol{x})$ in (5) is known as the minimum variance solution for $\boldsymbol{x}$. The multiple integral signs in (5) indicate integration over all dimensions of the state vector x. Using Bayes' Theorem (again following [33]), (6) may be rewritten as

$$\begin{aligned} \text{pdf}\,(\boldsymbol{x}) &\propto P(\boldsymbol{y} = \boldsymbol{y}_0 | \boldsymbol{x} = \boldsymbol{x}_{\text{true}})\, P(\boldsymbol{x} = \boldsymbol{x}_{\text{true}}) \\ &\propto P_{OS}[\boldsymbol{y}_0 - \boldsymbol{y}_s(\boldsymbol{x})]\, P_{as}(\boldsymbol{x} = \boldsymbol{x}_{\text{true}}) \end{aligned} \tag{7}$$

where P_{OS} is equivalent to the probability that the set of observations $\boldsymbol{y}_0$ deviate from the set of *simulated* observations $\boldsymbol{y}_s(\boldsymbol{x})$ by a certain amount, given the earth/atmosphere state $\boldsymbol{x}$. In future discussions P_{OS} will be called the probability of the observational deviation, and P_{as} the *a priori* probability that $\boldsymbol{x}$ is the true state of the earth/atmosphere.

If it is further assumed that the errors in the observations and the simulated observations are Gaussian and uncorrelated, then the probability of observational deviation can be expressed as

$$\begin{aligned} &P_{OS}[\boldsymbol{y}_0 - \boldsymbol{y}_s(\boldsymbol{x})] \propto \\ &\quad \exp\left(\{-0.5[\boldsymbol{y}_0 - \boldsymbol{y}_s(\boldsymbol{x})]^T\}\, (\boldsymbol{O} + \boldsymbol{S})^{-1} [\boldsymbol{y}_0 - \boldsymbol{y}_s(\boldsymbol{x})]\right) \end{aligned} \tag{8}$$

where $\boldsymbol{O}$ and $\boldsymbol{S}$ are the observation and model error covariance matrices, respectively. Substituting for P_{OS} in (7) using (8), and then using the resulting expression to substitute for pdf in (5), the final expression for the minimum variance solution is

$$\begin{aligned} E(\boldsymbol{x}) = \iint \cdots \int & \\ \cdot\, \boldsymbol{x}\, &\frac{\exp\{-0.5[\boldsymbol{y}_0 - \boldsymbol{y}_s(\boldsymbol{x})]^T\, (\boldsymbol{O} + \boldsymbol{S})^{-1}\, [\boldsymbol{y}_0 - \boldsymbol{y}_s(\boldsymbol{x})]\}}{A} \\ \cdot\, &P_{as}(\boldsymbol{x} = \boldsymbol{x}_{\text{true}})\, d\boldsymbol{x} \end{aligned} \tag{9}$$

where $\boldsymbol{A}$ is the normalization factor

$$\begin{aligned} \boldsymbol{A} = \iint \cdots \int & \exp\left(\{-0.5[\boldsymbol{y}_0 - \boldsymbol{y}_s(\boldsymbol{x})]^T\}\right. \\ &\left. \cdot\, (\boldsymbol{O} + \boldsymbol{S})^{-1} [\boldsymbol{y}_0 - \boldsymbol{y}_s(\boldsymbol{x})]\right) P_{as}(\boldsymbol{x} = \boldsymbol{x}_{\text{true}})\, d\boldsymbol{x}. \end{aligned} \tag{10}$$

2) Practical Simplification: At this stage, it is common practice in remote sensing applications to re-express P_{as} as the probability of the deviation of $\boldsymbol{x}$ from some suitable initial guess state $\boldsymbol{x}_{in}$ and then assume that the resulting probability $P_{in}(\boldsymbol{x} - \boldsymbol{x}_{in})$ has a Gaussian form. It follows that the minimum variance solution (7) is equivalent to the minimizing state $\boldsymbol{x}$ of the functional

$$\begin{aligned} J(\boldsymbol{x}) = &[\boldsymbol{y}_0 - \boldsymbol{y}_s(\boldsymbol{x})]^T\, (\boldsymbol{O} + \boldsymbol{S})^{-1}\, [\boldsymbol{y}_0 - \boldsymbol{y}_s(\boldsymbol{x})] \\ &+ (\boldsymbol{x} - \boldsymbol{x}_{in})^T\, \boldsymbol{I}^{-1} (\boldsymbol{x} - \boldsymbol{x}_{in}) \end{aligned} \tag{11}$$

where $\boldsymbol{I}$ is the covariance matrix of initial guess errors (see, e.g., [34]).

This method of solution requires the interactive search for the minimum of the scalar J in the multidimensional space of $\boldsymbol{x}$, which involves the evaluation of the partial derivatives of $\boldsymbol{y}_s$ at the current iterate of $\boldsymbol{x}$. However, this approach is not practical in the applications which follow. Firstly, the evaluation of $\boldsymbol{y}_s$ or its derivatives is computationally intensive (see Section II-B). Since in general the components of $\boldsymbol{y}_s$ are nonlinear functions of the vector components of $\boldsymbol{x}$, the derivatives of $\boldsymbol{y}_s$ must be evaluated on each iteration. Typically $\boldsymbol{x}$ can have a dimension $\sim$10 or greater, and $\boldsymbol{y}_s$ is also $\sim$10 in many applications; so $\sim$100 or more evaluations of $\boldsymbol{y}_s$ or its derivatives would be required on each iteration. In addition, for a given set of observations, J may have a shallow minimum or even multiple minima, which can complicate the search procedure. Another consideration is that in the applications of this study, the *a priori* probability distribution $P_{as}(\boldsymbol{x} = \boldsymbol{x}_{\text{true}})$, for which the components of $\boldsymbol{x}$ are typically hydrometeor water contents at different levels in the atmosphere, is decidedly non-Gaussian. Hydrometeor water contents usually follow a log-normal probability distribution (see [35]).

The alternative approach utilized in the present study is to make an approximate evaluation of the integral form of the minimum variance solution, (9). Firstly, a sufficiently large database of atmospheric profiles and associated brightness temperatures is generated using output of the GCE model (Section II-A) in conjunction with the forward passive microwave radiometer model (Section II-B). The impact of the database size and diversity of atmospheric profiles on the accuracy of profile retrievals will be examined in the next section. Using the large atmospheric profile/radiative database, the integral form of the minimum variance solution, (9) can be approximated by

$$\begin{aligned} &\hat{E}(\boldsymbol{x}) = \\ &\quad \sum_j \boldsymbol{x}_j\, \frac{\exp\{-0.5[\boldsymbol{y}_0 - \boldsymbol{y}_s(\boldsymbol{x}_j)]^T\, (\boldsymbol{O} + \boldsymbol{S})^{-1}\, [\boldsymbol{y}_0 - \boldsymbol{y}_s(\boldsymbol{x}_j)]\}}{A} \end{aligned} \tag{12}$$

where $\boldsymbol{A}$ is the normalization factor

$$\boldsymbol{A} = \sum_j \exp\left(\{-0.5[\boldsymbol{y}_0 - \boldsymbol{y}_s(\boldsymbol{x}_j)]^T\}\, (\boldsymbol{O} + \boldsymbol{S})^{-1}\, [\boldsymbol{y}_0 - \boldsymbol{y}_s(\boldsymbol{x}_j)]\right). \tag{13}$$

The integrals in (9) and (10) are replaced by the summations in (12) and (13) over all model simulated profiles ($\boldsymbol{x}_j$) in the atmosphere/radiative model database. Here the main assumption is that profiles in the model database occur with nearly the same relative frequency as those found in nature, or at least with the same frequency as those found in the region where the inversion method is to be applied. Under this assumption the weighting by $P_{as}(\boldsymbol{x} = \boldsymbol{x}_{\text{true}})$ in the integral form (9) is represented simply by the relative number of occurrences of a given profile type $\boldsymbol{x}_j$ in the summation (12). Since the profiles are simulated using a model which incorporates most relevant physical processes of the earth and atmosphere, the relative abundance of profiles of a certain type should be roughly the same as those of naturally-occurring profiles if a) the atmospheric model is used to simulate cloud development over the range of environments which are observed in the region of

interest, and b) that each cloud model simulation is sampled at regular time intervals, such that no particular stage of cloud or cloud system development is favored over another.

III. Retrieval Performance

It is possible to isolate the performance of the retrieval procedure by using synthetic data. The retrieval currently uses two distinct simulations to form its database. The first is the "GATE" simulation which developed in a very unstable environment and is known to contain large ice water contents [35]. Profiles are chosen from 5 model times at 126, 138, 174, 210, and 234 minutes into the simulation. The second model is a "TOGA/COARE" like simulation which contains much smaller ice water contents than the GATE simulations. Precipitation cells are tilted with respect to the vertical such that the heaviest rainfall rates are physically displaced from the maximum ice-water contents by as much as 20 km. Profiles from this simulation are chosen at 60, 90, 120, 150, 180, 210, and 240 min into the simulation. In the performance tests which follow, the TOGA profiles at 210 min into the simulation are used to represent the validation data. At this time, the system is mature and contains some of the strongest and most widespread rainfall. Brightness temperatures corresponding to this model time are treated as the "observed" brightness temperatures in the following studies. All simulations assume a "water" background.

Fig. 3(a)–(d) shows the retrieval performance using various data bases. The results correspond to retrievals at the highest sampling rate of the SSM/I (12.5 km) using the SSM/I channels and viewing angle. The particular format for displaying the retrieval results was chosen because it provides insight into the performance of the retrieval throughout the dynamic range of rainfall rates. The dependent database results shown in Fig. 3(a) use only profiles from the TOGA-210 minute simulation. The variable σ plotted is the width of the Gaussian distribution used to assign weights to individual profiles. As can be seen, results are almost perfect if sigma is small, but deteriorate quickly with increasing σ. The interpretation of this results is straightforward. Since all the "observed" profiles are contained in this dependent database, a small σ guarantees that only the true profile is selected and that few profiles with similar Tb but diverse structures are weighted in the final result. As σ gets larger, these more dissimilar profiles are weighted into the final structure and the results become less exact. Particularly, the retrieval is seen to overestimate the small liquid water contents up to $\sim$0.8 kg/m^2. This value corresponds to surface rainfall rates less than 3 mm/h. From 0.8 kg/m^2 to 3.5 kg/m^2 (3–15 mm/h), the retrievals for $\sigma = 1.5$ and 3.0 can be seen to follow the observations quite well. At higher liquid water contents, the retrieval is seen to systematically underestimate the observed values. Again, these results are not too surprising. At low rainfall rates, light uniform rain tends to have very similar brightness temperature signatures as heavier, more variable rain. Since these signatures are indistinguishable to a microwave sensor, the weighted average of profiles carried out by the retrieval tends to overestimate the very light rainfall amounts. At the high rainfall end, saturation of the brightness temperature signal is responsible for the underestimation.

TABLE II
Average Number of Structures Selected by Retrieval from a Suitable (TOGA) Database Compared to an Unsuitable (GATE) Database

Max. RMS	TOGA (avg. N)	GATE (avg. N)
1.5	2.46	0.06
3.0	47.75	0.72
6.0	443.02	34.39

Fig. 3(b) shows the same results discussed above, but using the independent "TOGA" structures to form the database (i.e., the "observations" are now excluded from the database of possible structures). The results can be seen to closely follow the trends discussed for the dependent database. A notable exception is the fact that a small value of σ no longer produces the almost perfect results. This is expected since the "observed" profiles are not available to the retrieval in this experiment.

Fig. 3(c) shows the retrieval results when only structures from the "GATE" simulation are made available to the retrieval. In this case, the retrievals are seen to perform rather poorly. This is due primarily to the fact that the database contains only candidate structures which are systematically different from the observed ones. This lack of fit leads to two questions: a) Given that any database will usually contain suitable as well as unsuitable profiles, can the retrieval select the appropriate ones? and b) Is there information in the brightness temperature differences that indicates poor performance due to a shortage of suitable structures? The first question can be answered in a straightforward manner using the "combined" database which includes all independent "TOGA" structures as well as the "GATE" structures. Fig. 3(d) reveals that the retrieval performs almost exactly as if only the independent "TOGA" structures had been used. The second question is related to expected errors in the retrieval. The fit of the database to the observations may be seen by simply counting the number of structures that are within a specified tolerance (in Tb) of the observations. If the database properly represents the observations, then the number of structures within this tolerance should be high. Conversely, if the database structures are vastly different from the observations, then the number of structures with similar brightness temperature vectors should be small. Table II lists the average number of structures within the prescribed tolerance for both the "TOGA" as well as the "GATE" database shown in Fig. 3(b) and (c). The tolerances are given in term of the rms Tb differences.

Table II shows that for a maximum rms deviations of 1.5 K, which corresponds roughly to the observational uncertainties, the "TOGA" database had an average of 2.5 structures that had a Tb vector similar to any observation. The "GATE" database, on the other hand, had virtually no structures, implying that on average, the database appears to fit the observations much

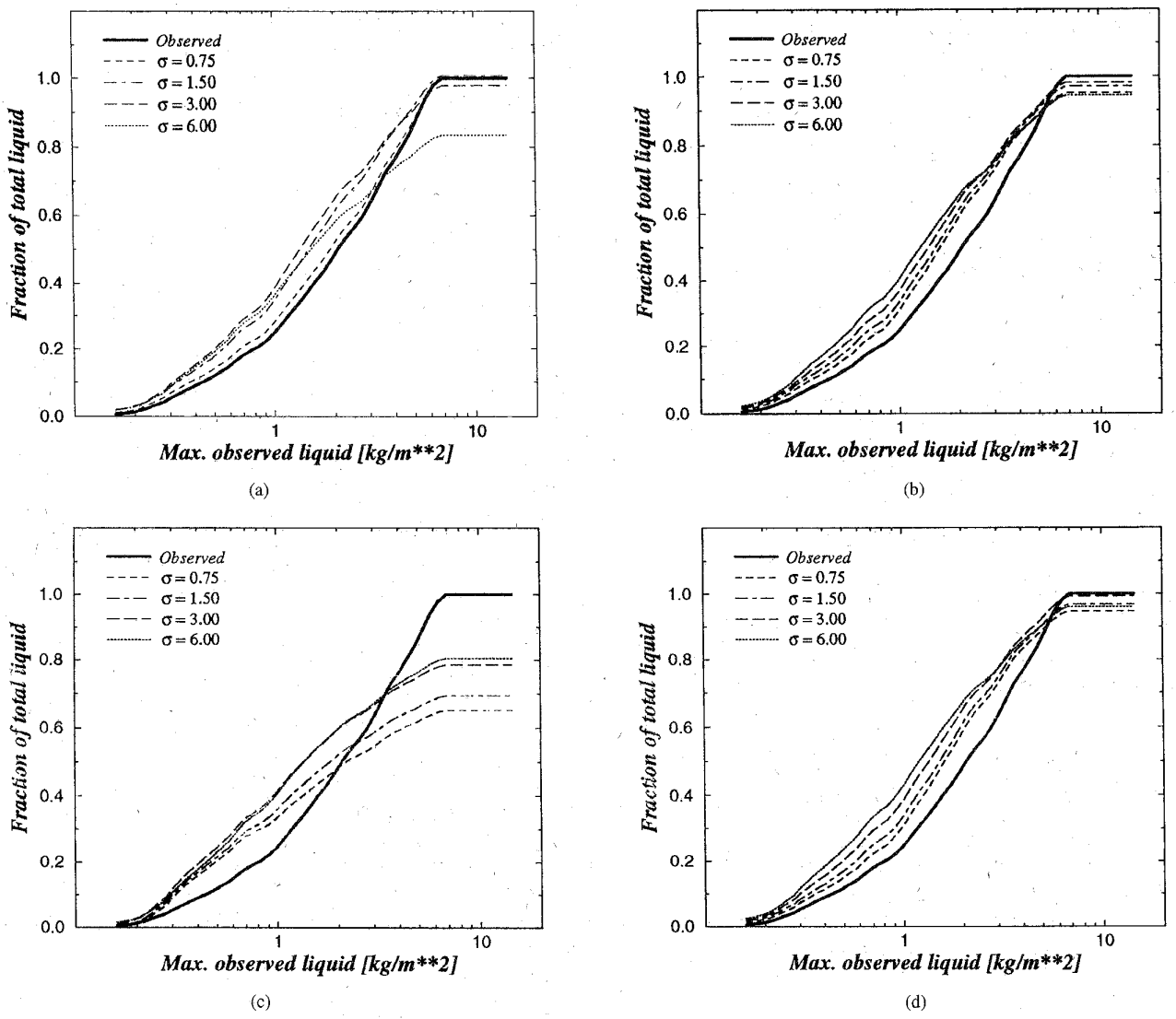

Fig. 3. Cumulative distributions of integrated precipitating liquid over a water background. Panels (a)–(d) show the relative retrieval performance using the indicated model database. The solid line indicates the known distribution from the 210 min TOGA/COARE simulation. Dashed lines represent various widths of the Gaussian function used to assign weights to individual profiles. Results shown are for 12.5-km retrievals using SSM/I channels.

less well than the "TOGA" simulation. Such information is valuable when assigning confidence levels to individual pixels.

Fig. 4(a) and (b) depict the retrieval results for surface rainfall rate and integrated ice respectively. The surface rainfall rate is defined as the precipitation liquid present in the lowest 0.5 km of the cloud structure. This retrieval is again seen to follow the pattern of the integrated liquid, except that the total errors appear somewhat larger. This is due to the fact that the passive microwave emission signal is better correlated with the integrated liquid than with the liquid at only the lowest 0.5-km layer. The integrated ice retrievals are considerably better than the liquid retrievals. This is due to the fact that the 85 GHz data which contains the greatest ice scattering signal, have resolution comparable to the resolution of the retrieval. The correlation is therefore not impaired by discrepancies between the true resolution of the sensor (~48 km for the 19 GHz emission signal) and the resolution of the retrieval.

Fig. 5 shows the same result as Fig. 3(d), except that the retrievals are performed for 25-km footprints matching the all-channel sampling resolution of the SSM/I. Comparing Fig. 5 with Fig. 3(d) shows that the two retrievals are again quite similar in tendency. The retrieval is better for 25-km footprints as should be expected because a much greater fraction of the energy from the rainfall scene is contained within a 25-km footprint than in a 12.5-km footprint.

Finally, Fig. 6(a) and (b) show results from this technique applied to the expected TRMM Microwave Imager (TMI) brightness temperatures. Fig. 6(a) uses only the channels of the SSM/I but with the improved resolution of the TMI due to the lower orbit of TRMM (350 km versus 833 for SSM/I). The results are for 10 km retrievals which correspond roughly to the all channel sampling rate of TMI. Results are improved over those shown in Fig. 3(d) (12.5-km resolution of SSM/I) and even Fig. 5 corresponding to the 25 km SSM/I retrievals.

TABLE III
SYNTHETIC RETRIEVAL PERFORMANCE SUMMARY. ALL VALUES CORRESPOND TO A WATER BACKGROUND

Fig.	Instrum.	Resol.	dbase	Parameter	rms error (% of mean)	correlation	bias (% of mean)
3a	SSM/I	12.5	Depend.	Tot. Liq.	68	0.81	0.9
3b	SSM/I	12.5	Toga	Tot. Liq.	74	0.77	- 1.8
3c	SSM/I	12.5	Gate	Tot. Liq.	101	0.60	- 21.3
3d	SSM/I	12.5	All	Tot. Liq.	75	0.77	- 0.9
4a	SSM/I	12.5	All	Sfc. Rain	91	0.79	0.7
4b	SSM/I	12.5	All	Tot. Ice	34	0.94	- 9.6
5	SSM/I	25.0	All	Tot. Liq.	48	0.88	1.0
6a	TMI[1]	10.0	All	Tot. Liq.	51	0.90	1.8
6b	TMI	10.0	All	Tot. Liq.	57	0.88	- 7.4

[1]excluding the 10-GHz channels.

Fig. 6(b) then shows the addition of the 10-GHz channel to the expected TMI retrievals. At this point, most of the underestimates at low rain rates as well as the underestimates at high rain rates have disappeared. This is due to the fact that the 10-GHz channel is virtually linear in the low rain rate domain and does not saturate as fast as the 19-GHz channel. The retrievals shown in Fig. 6(b) show good agreement with the observations up to $\sim$5 kg/m^2 which corresponds to a rainfall rate of $\sim$25 mm/h. At this point even the 10 GHz is near saturation. A small underestimation tendency can be seen in the figure.

To provide more quantitative assessments of the previous discussion, Table III presents summary values of rms errors, correlation coefficients and biases associated with each of the retrievals shown in Figs. 3–6. All tabulations are for $\sigma = 3.0$ K. In general, the values in Table III closely follow the trends shown in the figures. The notable exception are the results found in Fig. 6. Fig. 6(b) shows that adding the 10-GHz channel to the TMI produces significant improvements, while Table III shows that the rms errors and correlations actually decrease slightly. The explanation for this behavior may be tracked to the relatively poor spatial resolution of the 10-GHz channel. While the 10-GHz channel is useful to eliminate any systematic beam filling errors (thereby increasing the fit in Fig. 6(b), its signal stems from a footprint many times larger than the pixel being retrieved. The noise introduced by this discrepancies in resolution disappears when larger pixel areas are considered.

IV. AIRCRAFT STUDIES

During September and October 1993, a mini-experiment was conducted at the NASA Wallops Flight Facility called the Convection and Atmospheric Moisture Experiment (CAMEX) [37]. The ER-2 was instrumented with microwave, visible/infrared radiometers, and the ER-2 Doppler Radar System (EDOP). The AMPR instrument is a four-channel passive microwave sensor measuring 10.7, 19.0, 37.0, and 85 GHz. At nadir, the resolution of each channel is 2.8, 2.8, 1.5, and 0.6 km, respectively. Details of the instrument performance may be found in [38]. The EDOP system [39], [40] is a new radar system installed in the ER-2 to measure the vertical reflectivity and hydrometeor motions simultaneously. EDOP, located in the nose of the ER-2, is an X-band (9.6 GHz) Doppler radar with fixed nadir and forward-looking beams. The antennas have 3° beam widths which produce a spot size of about 1.2 km at the surface (assuming a 20-km aircraft altitude). For CAMEX, the system was configured for reflectivity measurements with 150 m gate spacing. The overall accuracy of EDOP during CAMEX was better than about 3 dB as determined from independent measures such as comparisons with the Melbourne, FL WSR-88D radar. On October 5, 1993, 18:33–18:40 UTC, the ER2 overflew a thunderstorm over an oceanic background. The EDOP measured reflectivities are shown in Fig. 7(a). The corresponding AMPR brightness temperatures at nadir are shown in Fig. 7(b).

All GCE model structures were used in the retrieval database for this case study. Due to the high resolution of the measurements, all profiles were kept at their original resolution (1.5 km for the "GATE" simulations and 1.0 km for the "TOGA" simulations). The small differences in sensor resolution for different channels was ignored. Brightness temperatures at the four channels were calculated to correspond to each cloud model structure. Fig. 7(c) shows the retrieved profiles generated from the four-channel AMPR data. In order

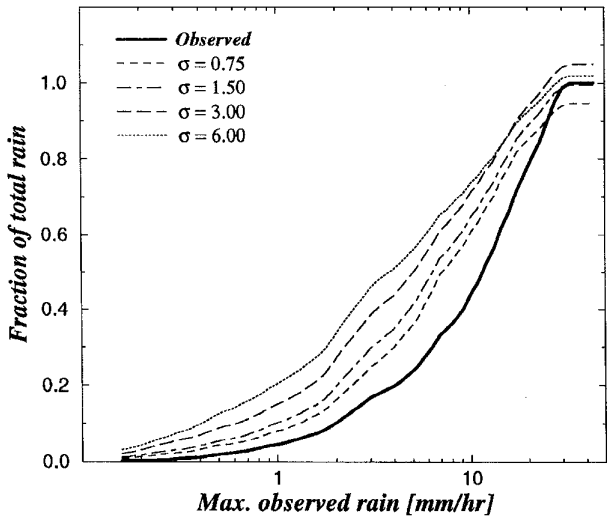

(a)

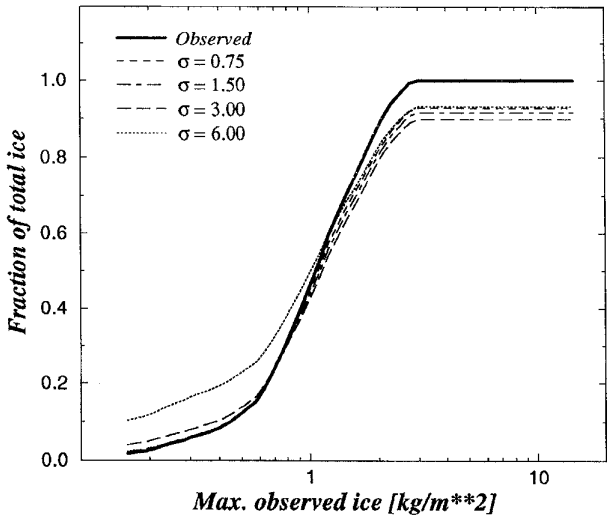

(b)

Fig. 4. Cumulative distributions of (a) surface rainfall and (b) integrated ice water content over a water background. The solid line indicates the known distribution from the 210 min TOGA/COARE simulation. All independent models are used in the retrieval database. Dashed lines represent various widths of the Gaussian function used to assign weights to individual profiles. Results shown are for 12.5-km retrievals using SSM/I channels.

to allow for direct comparisons with the validation data, hydrometeor profiles derived from GPROF were converted to equivalent reflectivities using the drop size distributions specified by the GCE model. Attenuation is accounted for. Quantitative comparisons between observed and retrieved vertical structures at 14 levels show that the retrievals have a bias of 2.97 dB with a mean error of 5.6 dB. Overall, the structures appear quite similar.

Two parameters are needed in order to run GPROF retrievals for which there is no theoretical guidance. The first of these is the relative weight assigned to each channel in comparing the GCE temperatures to the observations. In the current high-resolution implementation of GPROF, weights are assigned

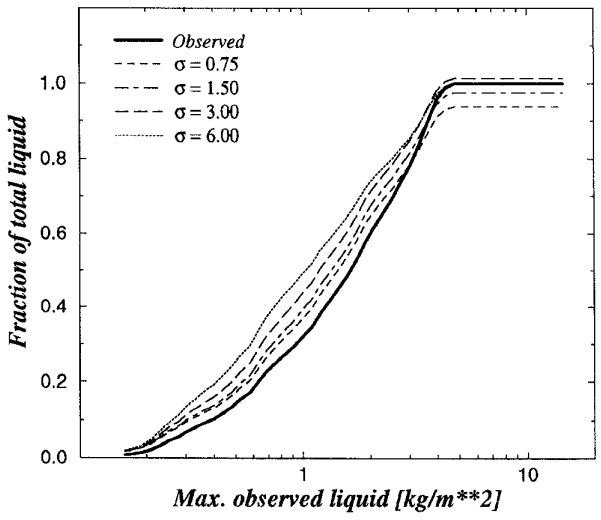

Fig. 5. Cumulative distributions of integrated precipitating liquid over a water background. The solid line indicates the known distribution from the 210 min TOGA/COARE simulation. Dashed lines represent various widths of the Gaussian function used to assign weights to individual profiles. Results shown are for 25-km retrievals using SSM/I channels.

using: wt $= \{\chi^2_{\rm obs} + \chi^2_{\rm sim}\}^{-1}$, where $\chi_{\rm obs} = 1.5$ K and $\chi_{\rm sim}$ is 2 K for 10 and 19 GHz, 3 K for 37 GHz, and 5 K for the 85-GHz channel. This particular choice of $\chi_{\rm sim}$ is consistent with the fact that higher frequency channels have larger noise in the simulations due to the uncertainties in the ice parameterization. These values produced consistently low rms errors in the synthetic satellite retrievals. While it might be possible to optimize the relative weights based upon validation data, it was felt that this might compromise the results presented here. The second parameter needed is the width of the Gaussian function, σ, used to assign relative weights to the individual profiles. The simulations shown in Section III showed that smaller values of σ generally produced better results. In applications to real data, however, it was found that setting σ too small tended to generate retrievals with occasional noisy spikes. This is due to the fact that when no structure is given sufficient weight (caused by small values of σ), then GPROF resorts to choosing the single structure with the smallest rms error. In order to avoid this undesirable noise, the value of σ was set to the smallest possible value which showed no visible noisy results. Satellite data led to a value of approximately 4 K and this value is again used here in order not to compromise the results with any case specific adjustments.

On October 5, 1993, 19:00–19:12 UTC, the ER2 overflew a precipitation event over a land background. The EDOP equivalent reflectivities and corresponding AMPR brightness temperatures at nadir are shown in Fig. 8(a) and (b), respectively. For land backgrounds, the high-resolution implementation of GPROF is applied in exactly the same fashion as over the oceanic background. Unlike the oceanic situation where a good radiometric response to hydrometeor content is seen at all frequencies, land background simulations generally show a pronounced response only to ice scattering at the higher frequencies (predominantly 85 GHz). Because of this

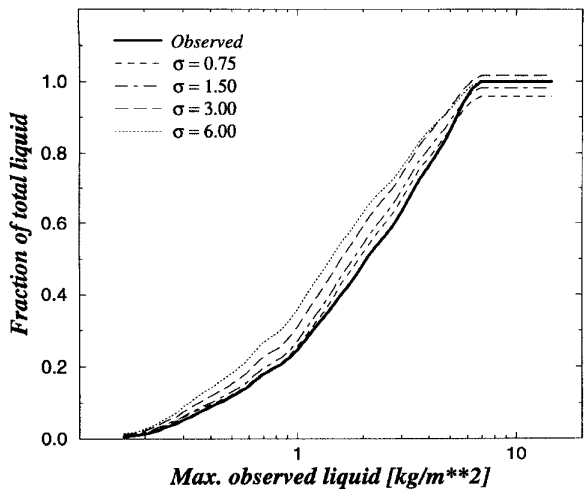

(a)

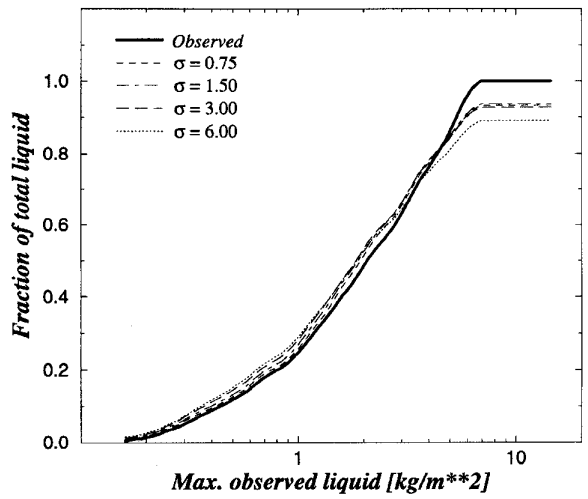

(b)

Fig. 6. Cumulative distributions of integrated precipitating liquid over a water background. The solid line indicates the known distribution from the 210 min TOGA/COARE simulation. Dashed lines represent various widths of the Gaussian function used to assign weights to individual profiles. Results shown are for 10 km retrievals using TRMM Microwave Imager channel resolutions without [panel (a)], and with [panel (b)] the addition of the 10-GHz channels.

behavior, it is expected that over land, the retrieved profiles will depend strongly on the observed 85 GHz scattering signature regardless of the channels used to compare the observed and simulated radiances. Results from GPROF are shown in Fig. 8(c). It is immediately evident that most of the features seen in the radar reflectivity image are not properly captured by the retrieval. Closer inspection of the AMPR brightness temperatures reveals the cause for this behavior. Fig. 8(b) shows that there is virtually no signal, even in the 85-GHz channel for this rain event. The bias in this retrieval was −0.33 dB and the mean error was 8.1 dB. Overall, the retrieved structures cannot be said to produce an acceptable rendering of the observed reflectivity field.

This example over land, although perhaps not typical of convective storms which show a reasonable correlation between rainfall and ice scattering, illustrates the shortcoming of passive microwave retrievals over land. For global satellite applications, the database of structures used by GPROF is therefore limited to the "GATE" simulations. The rational for restricting the database to these simulations is that the "GATE" profiles have been used extensively in the Goddard Scattering Algorithm (GSCAT) (see [3]) and tend to produce global mean values in fairly good agreement with raingauge observations. It should be made clear that these agreements are for a large scale area averages—not for a pixel by pixel agreement. The frequent lack of a coherent rainfall signal over land, as demonstrated above, ultimately makes accurate instantaneous retrievals over land very difficult if not impossible.

V. Satellite Studies

The general methodology of the retrieval was discussed in detail in Section II. For global applications, however, certain additional steps are taken before the retrieval is applied. Over oceans, these steps consist of eliminating cloud free regions from consideration. This is done to improve the computational efficiency of the algorithm. Over land backgrounds, the algorithm not only screens pixels for apparent cloud free conditions (warm 85 GHz brightness temperatures), but it also screens pixels which are thought to be contaminated by snow or ice on the surface. The relative channel weights are also modified to account for the larger uncertainties due to the background radiances associated with larger footprints. Over water χ_{sim} is set to 4.0 K for 19 GHz, 4.5 K for 22.235 GHz, 5.0 K for 37 GHz, and 6.0 K for 85 GHz. Over land, the uncertainties of the surface become more pronounced and the channel weights are used to reflect that. For land retrievals, χ_{sim} is set to 7.5 K for 19 GHz and 22.235 GHz, 6.0 K for 37 GHz, and 4.0 K for 85 GHz. This weighting reflects the fact that higher frequencies are less likely to penetrate to the surface and thus less likely to be contaminated with surface noise. As mentioned previously, only the "GATE" simulation is used to construct the database over land because the tilted nature of the "TOGA" simulations render relationships between ice scattering and rainfall meaningless. Over coastlines, the retrieval uses the land database, but only the 85 GHz–H channel is given any weight. This was done because any advantage in using lower frequency channels to help quantify large scattering events is offset by the fact that uncertain fractions of land and water background in the pixels make quantitative interpretation of the lower frequency channels virtually impossible.

One additional step was implemented for global retrieval purposes. This step serves as a quality control flag when GPROF finds no suitable structures from which to generate a results. In these situations, GPROF uses the nearest available structure in an rms sense and notes the deviation between observed and retrieved brightness temperatures. Before a given profile is considered final, however, GPROF sets all pixels with excessive rms errors to no-rain and then applies a median filter to the data. The median filter operates on the pixel and the 8 surrounding ones. This procedure will eliminate spurious rain signals that may be due to such things as small islands or defects in the data itself. It does not, however, adversely

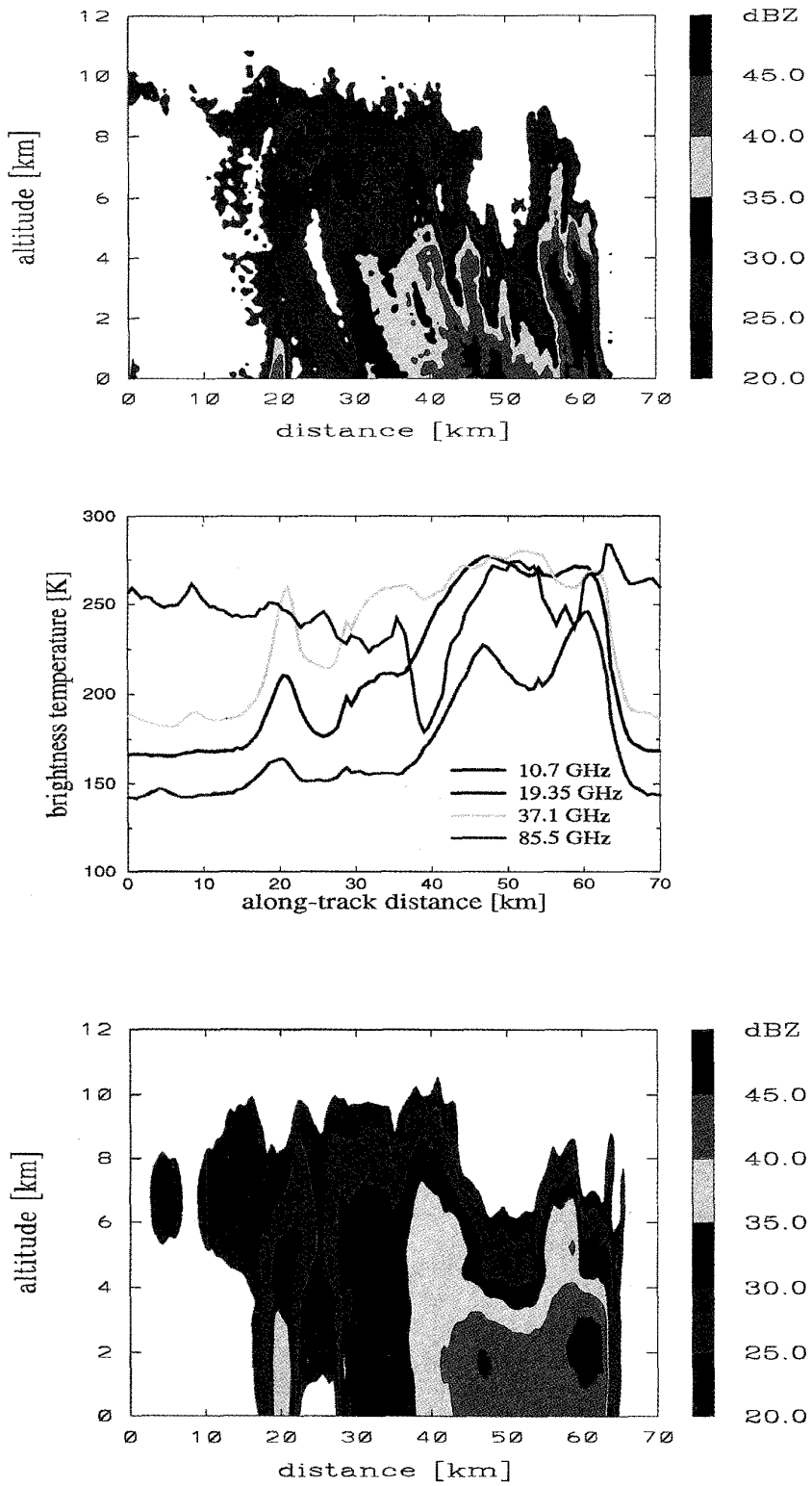

Fig. 7. Top panel: EDOP measured reflectivity structure. Center panel: AMPR observed brightness temperatures, at nadir, coincident with EDOP measurements. Bottom panel: Retrieved radar reflectivity from GPROF algorithm. Reflectivities are determined from the cloud model prescribed drop-size distributions. Background is water.

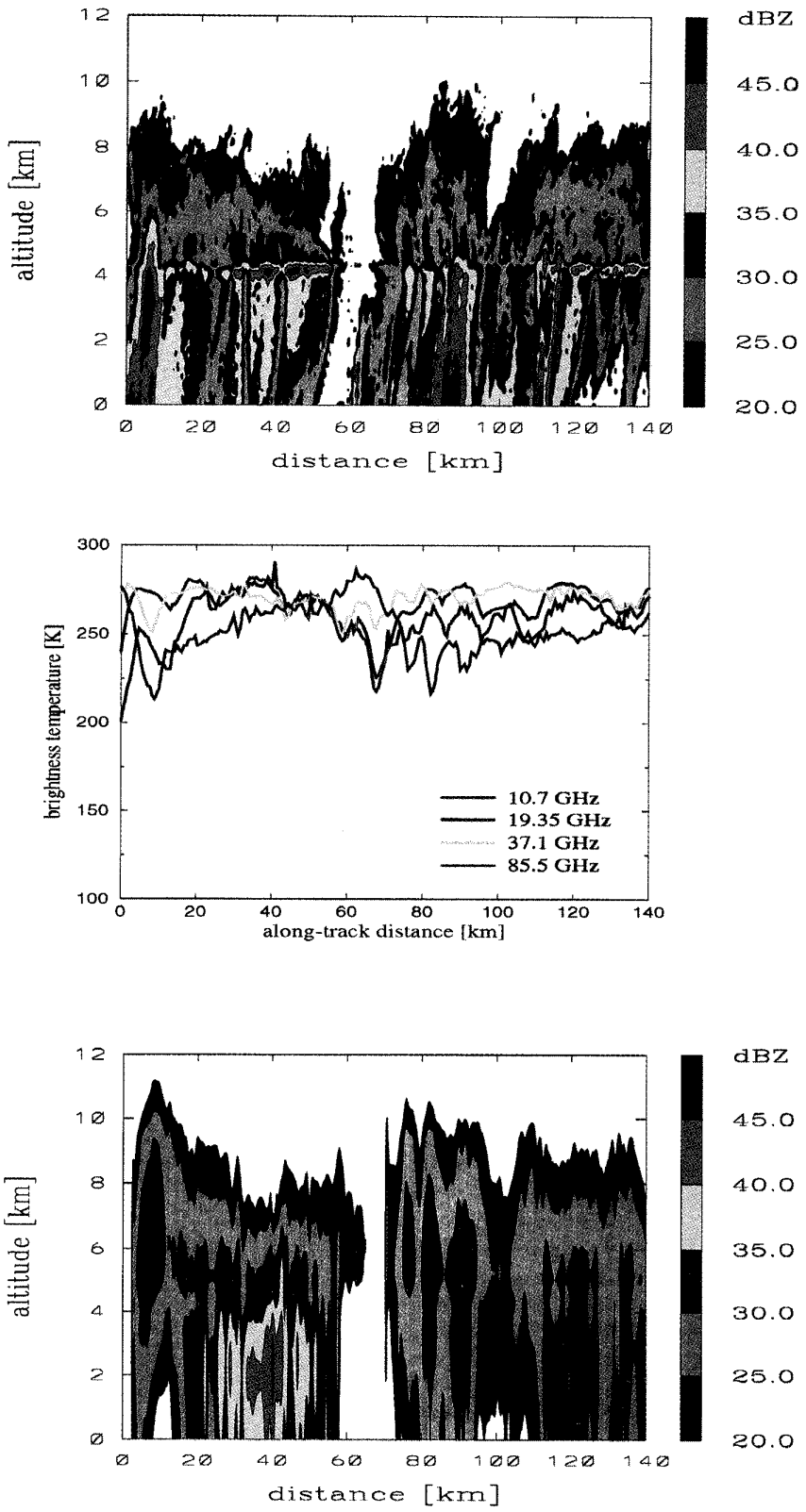

Fig. 8. Top panel: EDOP measured reflectivity structure. Center panel: AMPR observed brightness temperatures, at nadir, coincident with EDOP measurements. Bottom panel: Retrieved equivalent radar reflectivity from GPROF algorithm. Reflectivities are determined from the cloud model prescribed drop-size distributions. Background is land.

TABLE IV
COMPARISON OF GPROF GLOBAL RAINFALL ESTIMATES WITH GSCAT AND GPCP RESULTS. COMPARISONS ARE FOR OCEANS ONLY

A	B	Res.	N_{obs}	<A> [mm/mo.]	<B> [mm/mo.]	Corr.	RMS diff. [mm/mo.]
GPROF	GSCAT	2.5°	2155	82.0	87.9	0.934	51.7
GPROF	GPCP	2.5°	2155	82.0	119.6	0.924	65.7
GSCAT	GPCP	2.5°	2155	87.9	119.6	0.888	74.3
GPROF	GSCAT	5.0°	571	82.0	88.5	0.954	38.7
GPROF	GPCP	5.0°	571	82.0	117.0	0.945	57.3
GSCAT	GPCP	5.0°	571	88.5	117.0	0.919	60.2

affect pixels imbedded in areas of precipitation where the cloud structure database may have been underpopulated. While this solution may not be ideal, the thrust of GPROF was to develop a very simple, logically structured profiling algorithm which could serve as a basis for future enhancements. Work such as that of [11], or [12], which iteratively modify the profiles to minimize the Tb differences are undoubtedly worth exploring in these situations. Until the extent of the improvement can be demonstrated, however, the main goal of this algorithm is to preserve the simplicity and transparency that the current solution offers. Fig. 9 shows a schematic flow diagram of GPROF as it is currently implemented.

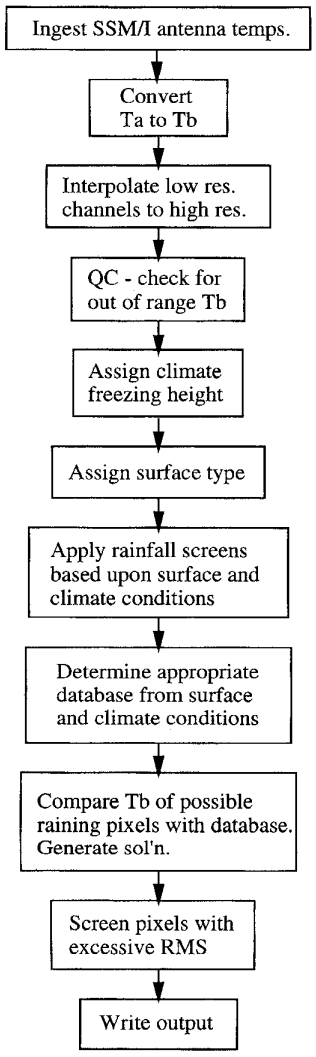

Fig. 9. Schematic flow diagram of GPROF algorithm.

A. Global Applications

Rainfall estimates were made using GPROF in order to compare it to existing algorithms whose properties have been documented. These algorithms are GSCAT [3], which is a scattering algorithm using primarily the 85-GHz horizontal polarization, and the emission algorithm used for the GPCP project [2] which uses primarily the 19-GHz emission channel. The emission algorithm works over water only. Because GPROF is currently limited to tropical environments. (This is dictated by the availability of trustworthy cloud dynamical model simulations.) Therefore, only those areas whose climatological surface temperature is greater than 296 K are retrieved by GPROF. Results of the three algorithms are shown in Fig. 10. As can be seen, the algorithm agree quite well in the broad sense of where the precipitation maxima occur. Fig. 11 shows the relation among individual grid elements, at 2.5° resolution, among the three algorithms. Quantitative comparisons between the three algorithms (where all three have data) are presented in Table IV.

While comparisons with ground based validation data may contain significant scatter due to the sampling limitations of the satellite, the scatter in these diagrams is due entirely to differences in the physical interpretation of the radiometric signal. The rms differences between the algorithms is still ~66% of the mean monthly accumulations for 2.5° grid boxes and ~54% for 5° grid boxes. These differences are substantial. Thus, while the global rainfall maps seem to be in good qualitative agreement, that agreement cannot be translated into agreements on the physical interpretation of rain signals. The fact that the correlations between GPROF/GSCAT and

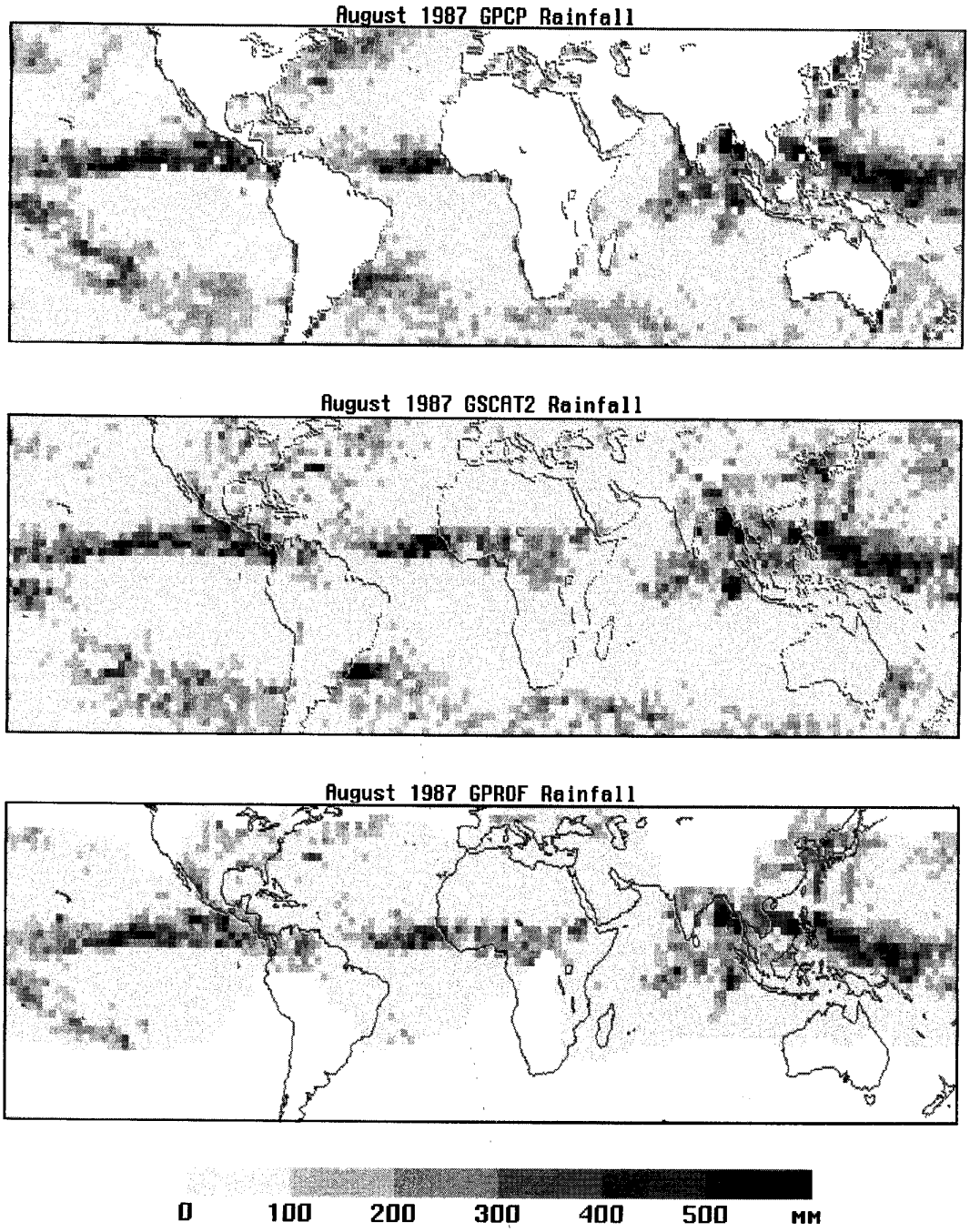

Fig. 10. Top panel: Global (50° N-50° S) monthly rainfall accumulations at 2.51° resolution obtained from an "emission" algorithm. Center panel: A "scattering" algorithm. Bottom Panel: The current "profiling" algorithm.

GPROF/GPCP are higher than GSCAT/GPCP is an indication that GPROF is making use of both emission as well as scattering signatures.

B. Darwin Case Study

To test of the algorithm performance, a two month period covering February and March 1988 over Darwin, Australia, was selected. Validation data is available from the Darwin 5-cm radar and a network of rain gauges which served to calibrate the reflectivity–rainfall relationships. These cases were also compared in a previous profiling algorithm [40]), henceforth referred to as [40] and thus serve as a reference to earlier results. Table V presents the summary statistics of the intercomparison.

While the results from the current algorithm very much follow the pattern of results shown in [40], the results are not

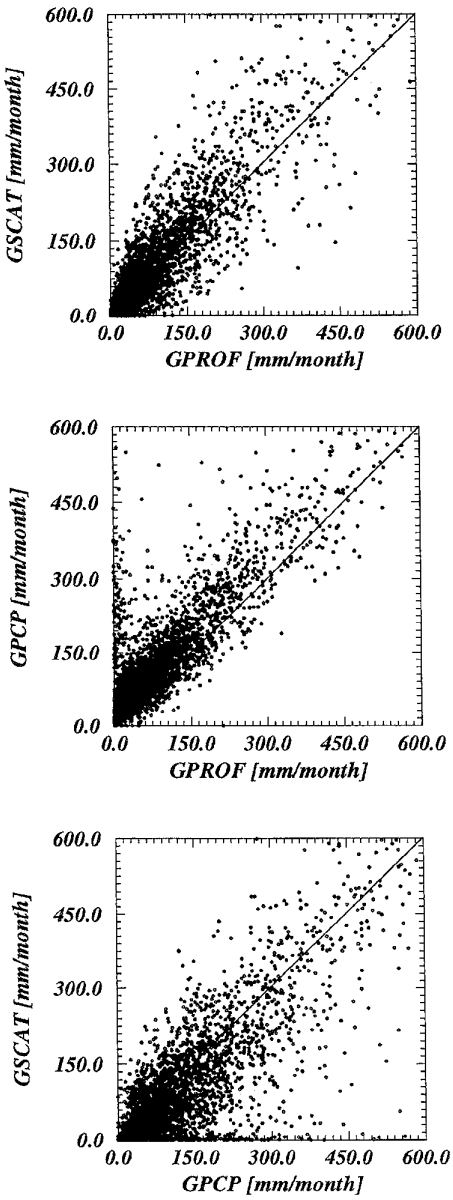

Fig. 11. Scatter diagram of monthly rainfall corresponding to 2.5° grid elements shown in Fig. 10. Top panel: Relationship between "scattering" and "profiling" algorithms. Center panel: Relationship between "emission" and "profiling" algorithms. Bottom panel: Relationship between "scattering" and "emission" algorithms.

identical. First of all, the Z–R relationship used to convert radar reflectivities was modified from $Z = 170R^{1.5}$ used in [40] to $Z = 167R^{1.25}$. This change was suggested by [40], who did a careful analysis of the Darwin radar data for February 1988. In that analysis they found that the $Z = 170R^{1.5}$, which was originally derived from disdrometer data, underestimated the rainfall when compared to the raingauge network. A second difference is that GPROF was not able to achieve the extremely high correlations achieved by [40] (0.966) over water. This may be due to the heritage of [40] in which model structures were in large part developed to get good correlations with available radar data. Since Darwin represents one of only a few sites with reliable ground based radar data, this undoubtedly had a major impact upon the structures available to the retrieval and thus on the correlations achieved at Darwin. GPROF structures are derived solely from the numerical models and are thus completely independent of the Darwin data. While the correlations are not as high as they were for [40], there is good reason to expect these results to be more globally representative than the [40] results. For pixels over water, it should also be mentioned that part of the lower correlation stems from an overestimate of precipitation during monsoon events that generated large areas of relatively uniform precipitation. We believe the overestimate (seen also in the synthetic data) to be the result of poor spatial resolution. More work is needed to determine the specific effects of antenna pattern deconvolution schemes and adding spatial information in the form of horizontal variability to address the poor horizontal resolution problem. To compare the vertical structure retrieved by GPROF, we again follow the example used by [40]. Fig. 12(a) and (b) show the surface rainfall inferred by GPROF and the Darwin radar, respectively. The vertical structure along the dashed line [shown in Fig. 12(a) and (b)] inferred by GPROF is shown in Fig. 12(c) while the measured vertical cross section is shown in Fig. 12(d). Aside from the poor spatial resolution inherent in the SSM/I retrievals, the two vertical cross sections can be seen to show fairly good agreement.

TABLE V
SUMMARY STATISTICS FOR DARWIN VALIDATION STUDY

	Water	Coast	Land
N. obs	152	148	52
mean rainfall (GPROF)	0.268	0.310	0.319
mean rainfall (radar)	0.279	0.483	0.457
bias	−0.09	−0.173	−0.138
rms error	0.517	0.537	0.712
correlation	0.800	0.733	0.882

Over land, the correlations achieved with GPROF are higher than the [40] results. This appears to be due to the fact that GPROF has a greater reliance upon the 85-GHz channel over land than the [40] algorithm. Correlations are thus higher although the bias and rms errors are similar to previous results. Over coastlines, the correlations are lower than previously. The difference is largely due to a procedural change. [40] treated all coastlines pixels as either water or land background. While this caused some problems for pixels positioned over the actual coastline, it allowed for reasonable retrievals of those pixels which were either over water or land. GPROF uses only the 85-GHz scattering signal over all pixels classified as coastline. While this procedure appears to degrade the results somewhat, it is consistent with the philosophy of GPROF that the behavior of the algorithm be completely predictable.

C. TOGA/COARE

As a final example, we compare the results from GPROF to the shipborne radar data obtained during TOGA/COARE.

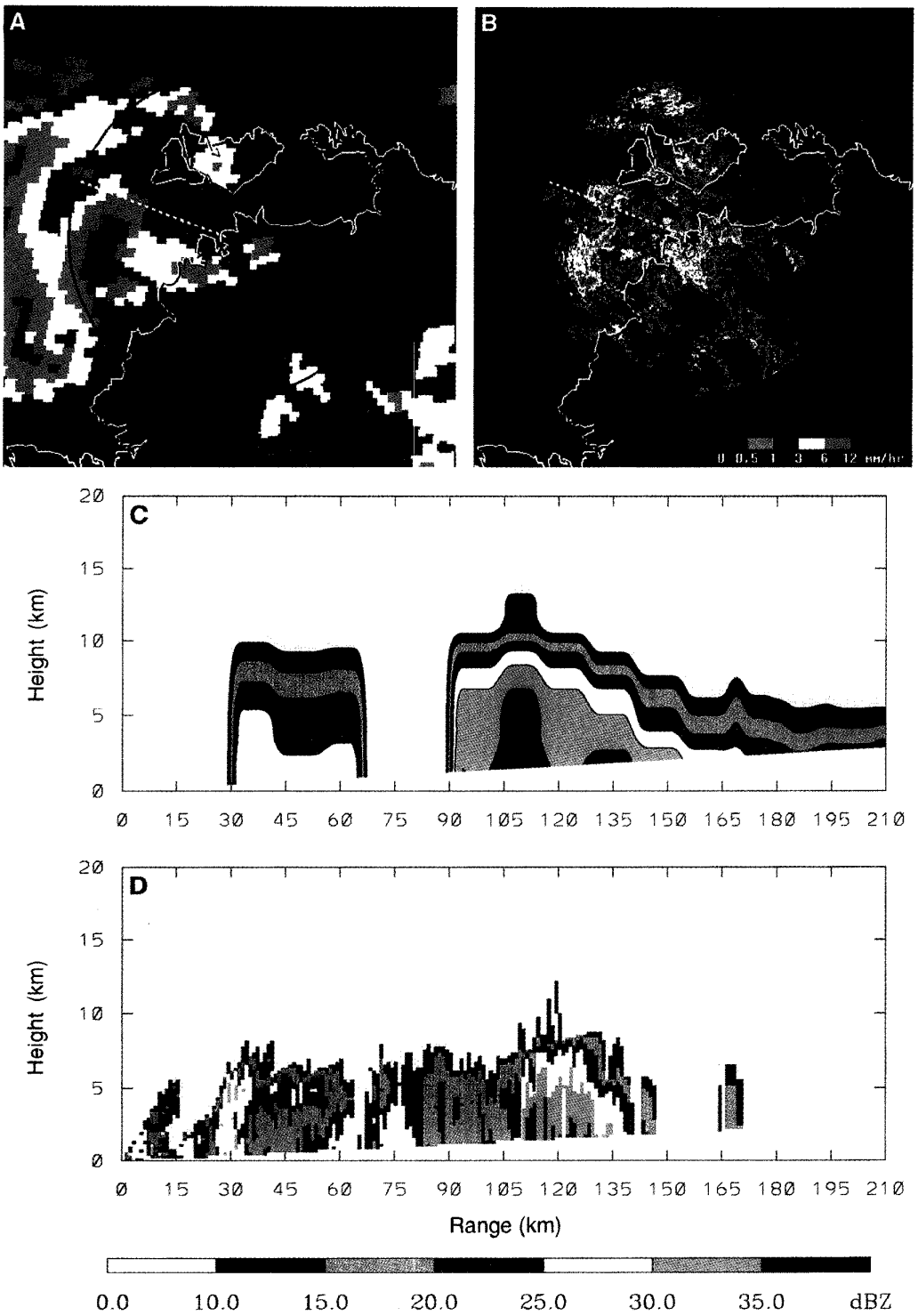

Fig. 12. Retrieved rainfall compared to ground-based radar for a case study over Darwin, Australia, at 09:35 UTC 27 March 1988. (a) Retrieved surface rainfall from SSM/I. (b) Radar-derived rainfall. (c) Cross section of reflectivities along $\theta = 290°$ [shown in panels (a) and (b)] as derived from the retrieval algorithm. (d) Measured radar reflectivities along $\theta = 290°$.

Comparison of all coincident pairs of satellite and radar pairs, averaged to 0.5° resolution are presented in Table VI. To first order, it can be seen that GPROF significantly overestimates the validation data for Cruises II and III. Because the vast majority of algorithms, both microwave as well as infrared, overestimated the rainfall over the TOGA/COARE region

TABLE VI
COMPARISONS BETWEEN SURFACE RADAR OBSERVATIONS AND GPROF RAINFALL RATES FOR THE 3 CRUISES OF TOGA/COARE. VALUES IN () CORRESPOND TO [40] RESULTS

	Cruise I	Cruise II	Cruise III
N pixels (0.5°)	1212 (1222)	1737 (1715)	1637 (1617)
Mean radar [mm/hr]	0.103 (0.100)	0.197 (0.192)	0.130 (0.136)
Mean satellite [mm/hr]	0.066 (0.098)	0.527 (0.453)	0.238 (0.217)
RMS error [mm/hr]	0.231 (0.461)	1.479 (1.284)	0.753 (0.889)
Correlation Coef.	0.788 (0.683)	0.666 (0.703)	0.707 (0.554)

by margins similar or greater than GPROF (see [42]), the validation data itself may be questionable. For the 4 months covered by the shipborne radars, the GOES Precipitation Index, (GPI), generated a mean rainfall of 322 mm/month compared to 109 mm/month derived from the radars. While there is currently no real evidence to identify the source of the discrepancy, recent attention has been given to the vertical structure of the precipitation. Initial results from the wind profiler at Kapingamarangi atoll suggest that the mean reflectivity of convective precipitation decreases by ~1 dB/km from the surface. Such a vertical structure could have a significant impact upon the total rainfall estimated from the shipborne radars if the climatological decrease of reflectivity with height were not accounted for. A second source for significant discrepancies might be the general abundance of stratiform precipitation, particularly during Cruise II, reported by the TOGA participants. The emission signatures of large stratiform regions tend to be greater than the equivalent emission for highly variable rain fields.

As can be seen from Table VI, the estimates of GPROF are significantly higher than the shipborne radar estimates for Cruises II and III. This problem, as discussed above, may be related to the radars. Comparing GPROF to the earlier estimates of [40], it can be seen that the rms errors and correlations are better for GPROF during Cruises I and III while [40] performed slightly better during Cruise II.

VI. CONCLUSION

This paper has focused primarily upon the surface rainfall generated by the GPROF algorithm because it is the quantity which is most easily verifiable. Quantitative vertical structure which is associated with the precipitation was only shown in two examples using aircraft data and one example using SSM/I data and the Darwin, Australia radar. Overall, the results appear very encouraging despite the fact that GPROF has not undergone any rigorous optimization based upon surface radar products. The overall performance of GPROF was found to be similar to a previous algorithm developed by [39] and [40] that used hypothetical structures rather than dynamically derived structures from the GCE model. For the Darwin validation study, the overall biases remained roughly constant between the two algorithms. Correlations decreased somewhat over water backgrounds but increased over land. The decrease over water background could be explained by the fact [40] that structures had considerable heritage from the Darwin area while GPROF structures are completely independent of the validation data. Over land, the greater reliance of GPROF upon the scattering channels led to somewhat better correlations there. The atoll case study, although not specifically shown in [40], revealed that GPROF produces generally higher rainfall accumulations than [40] by approximately 10%. Since both GPROF and [40] underestimate the atoll gauge accumulations (GPROF underestimates the atoll accumulations for August 1987 by 22.7%) the higher rainfall accumulations from GPROF probably represent an improvement. The fact that sampling errors play such an important role in comparing monthly accumulations from sparsely sampled satellite data over 2.5° with continuously sampled point measurements make it necessary to qualify the last statement. For the TOGA/COARE comparison, the most important result is the large discrepancy between satellite and ship-borne radar estimates. The fact that there is general agreement among the various satellite techniques, however, casts some doubts as to the overall magnitude of the radar estimates. From an overall bias point of view, GPROF is near the median of all submitted algorithms. The correlations achieved with GPROF versus [40] are mixed. GPROF had significantly higher correlations for Cruises I and III while the correlation decreased somewhat for Cruise II. Compared to the other algorithms submitted to AIP3, GPROF correlations are better than average for Cruises I and III but below average for Cruise II.

The ability to properly retrieve the precipitation profiles using GPROF depends in large part upon the information content of the brightness temperature signal. Over land, where the signal is dominated by the 85-GHz scattering signature, the algorithm in essence always retrieves the mean hydrometeor structure as determined by the cloud models, which corresponds to the integrated ice content observed by the 85-GHz channel. Over water where more radiometric signal is available, the algorithm is able to discern far more structure information as shown in Fig. 7. Careful inspection of the SSM/I based over-water retrievals shown in Fig. 12, however, indicate that much of the fine structure apparent from the aircraft retrievals is not evident in the satellite retrievals. This loss of vertical structure information is related to the relatively large pixels of the SSM/I. The inevitable mixture of rain systems in various stages of development causes a decrease in the number of independent channels which in turn is reflected in the retrieved vertical structure. The improved spatial resolution of TRMM, will therefore be the key element for obtaining improved hydrometeor profiles in the future.

GPROF was designed primarily with operational goals of TRMM in mind. To that end, it was designed to meet two key requirements. The first requirement is that GPROF be computationally modest. In its current implementation, one month of SSM/I data can be processed in ~24 h on a midsize workstation. This substantial gain over previous profiling algorithms has been achieved primarily by eliminating explicit radiative transfer computations from inside the retrieval scheme. While this procedure may occasionally sacrifice the algorithm's ability to obtain an ideal match between observed and modeled Tb, the algorithm benefits by being able to make use of the best available radiative transfer schemes without

concern for time required by these calculations. This allows GPROF to use the intrinsic variability of the cloud model fields in the retrieval rather than making *a priori* adjustments for the rainfall inhomogeneity. The second requirement is that GPROF be structured so individual processes within the retrieval are clearly separated and their effect upon the final result is both predictable and quantifiable. This design is meant to facilitate incremental improvements by allowing effects of specific refinements to be clearly documented.

One shortcoming of GPROF which affects the correlations particularly during Cruise II, but is also evident at Darwin and in the synthetic retrievals is the apparent overestimate of rainfall intensity near the surface when large areas of either moderate stratiform rain or light stratiform rain with embedded convection dominate the scene. In these cases, GPROF produces rainfall values as much as 2–3 times larger than the surface radars. While these regions may be affected most strongly by attenuation in surface radars, evidence of this behavior in the synthetic data suggests that the problem is related to poor spatial resolution. To that end, continuing research will focus on: a) using antenna deconvolution schemes to improve the resolution of the low-frequency channels; b) making use of the horizontal inhomogeneity in the channel data to help in selecting profiles for the retrieval; and c) investigating whether channel combinations or differences (e.g., emission and scattering indices described by [9]) carry more information pertaining to the nature of the rainfall. The quantifiable goal of these enhancements is to obtain a better separation between convective and stratiform rainfall.

One aspect of GPROF mentioned only briefly in this paper is its ability to incorporate data from passive microwave sensors such as the TRMM Microwave Imager (TMI) with the remainder of the TRMM rainfall complement: the Precipitation Radar (PR) and Visible and Infrared Radiometer (VIRS) and the Lightning Sensor (LIS). For the PR, radiative transfer calculations may be performed to predict the cloud model reflectivities. These predicted values may then be compared at each range gate to the observed values of reflectivity and a rms difference can be constructed in the same fashion as described here. A combined retrieval then consists simply of choosing the optimal weights with which to combine radiometer and radar information. Reference [43] has applied this technique to a combination of airborne radar and radiometer data. The same procedure can be applied using the VIRS information. The lightning information is more difficult to use directly because no explicit information is present in the cloud dynamical model to indicate which profiles could potentially be associated with lightning events. If a correlation between individual profiles and their capacity for producing lightning can be found, however, then lightning too could be added as a criteria for weighting structures in the retrieval.

The greatest benefit from a profiling algorithm such as GPROF will come when latent heating profiles can be supplied along with the hydrometeor structures. Cloud heating profiles can be deduced by assigning characteristic profiles to the convective and stratiform precipitation components and renormalizing them by the retrieved surface rainfall rates [44], [46]. The relative portions of convective and stratiform precipitation over a given region will be of great interest to climate modelers due to the differences in the cloud heating/moistening and radiative effects associated with each type of precipitation [46], [47]. Heating and moistening profiles (Q1 and Q2) can also be obtained by associating the GCE model heating and moistening profiles directly with each hydrometeor column in the retrieval process. Heating budgets, however, are associated with not only the hydrometeor structure, but with the dynamics of the storm evolution as well. More research is therefore needed to define minimum areas over which such a procedure is likely to produce acceptable solutions.

ACKNOWLEDGMENT

The authors wish to thank R. Adler, A. Chang, G. Heymsfield, J. Caylor, and R. Hood for contributing data needed by this study. The authors also wish to thank the GCE development team of W.-K. Tao, B. Ferrier, S. Lang, and Y. Wang.

REFERENCES

[1] J. Simpson, C. Kummerow, W. K. Tao, and R. F. Adler, "On the tropical rainfall measuring mission (TRMM)," *Meteor. Atmos. Phys.*, to be published.

[2] T. T. Wilheit, A. T. C. Chang, and L. S. Chiu, "Retrieval of monthly rainfall indices from microwave radiometric measurements using probability distribution functions," *J. Atmos. Ocean. Tech.*, vol. 8, pp. 118–136, 1991.

[3] R. F. Adler, G. J. Huffman, and P. R. Keehn, "Global tropical rain estimates from microwave-adjusted geosynchronous IR data," *Remote Sensing Rev.*, vol. 11, pp. 125–152, 1994.

[4] N. C. Grody, "Classification of snow cover and precipitation using the special sensor microwave imager," *J. Geophys. Res.*, vol. 96, pp. 7423–7435, 1991.

[5] C. Kidd and E. C. Barrett, "The use of passive microwave imagery in rainfall monitoring," *Remote Sensing Rev.*, vol. 4, pp. 415–450, 1990.

[6] P. Bauer and P. Schluessel, "Rainfall, total water, ice water and water vapor over the sea from polarized microwave simulations and SSM/I data," *J. Geophys Res.*, vol. 98, pp. 20737–20759, 1993.

[7] W. S. Olson, F. J. LaFontaine, W. L. Smith, R. T. Merrill, B. A. Roth, and T. H. Achtor, "Precipitation validation" in *DMSP Special Sensor Microwave/Imager Calibration/Validation Final Report Volume II.* Washington, DC: Naval Res. Lab., 1991, pp. 1–40.

[8] G. Liu and J. Curry, "Retrieval of precipitation from satellite microwave measurements using both emission and scattering," *J. Geophys. Res.*, vol. 97, pp. 9959–9974, 1992.

[9] G. W. Petty, "Physical retrievals of over-ocean rain rate from multichannel microwave imagery. Part I: Theoretical characterizations of normalized polarization and scattering indeces," *Meteor. Atmos. Phys.*, vol. 54, pp. 79–99, 1994.

[10] C. Kummerow and L. Giglio, "A passive microwave technique for estimating rainfall and vertical structure information from space, Part I: Algorithm description" *J. Appl. Meteor.*, vol. 33, pp. 3–18, 1994.

[11] E. A. Smith, X. Xiang, A. Mugnai, and G. J. Tripoli, "Design of an inversion-based precipitation profile retrieval algorithm using an explicit cloud model for initial guess microphysics," *Meteor. Atmos. Phys.*, vol. 54, pp. 53–78, 1994.

[12] A. Mugnai, E. A. Smith, and G. J. Tripoli, "Foundations for physical-statistical precipitation retrieval from passive microwave satellite measurements. Part II: Emission source and generalized weighting function properties of a time dependent cloud-radiation model," *J. Appl. Meteor.*, vol. 32, pp. 17–39, 1993.

[13] W.-K. Tao and J. Simpson, "Goddard cumulus ensemble model. Part I: Model description," *TAO*, vol. 4, pp. 35–72, 1993.

[14] S.-T. Soong and W.-K. Tao, "A numerical study of the vertical transport of momentum in a tropical rainband," *J. Atmos. Sci.*, vol. 41, pp. 1049–1061, 1984.

[15] W.-K. Tao and S.-T. Soong, "A study of the response of deep tropical clouds to mesoscale processes: Three dimensional numerical experiments," *J. Atmos. Sci.*, vol. 43, pp. 2653–2676, 1986.

[16] Y.-L. Lin, R. D. Farley, and H. D. Orville, "Bulk parameterization of the snow field in a cloud model," *J. Clim. Appl. Meteor.,* vol. 22, pp. 1065–1092, 1983.
[17] M.-D. Chou and A. Arkin, "Computation of infrared cooling rates in the water-vapor bands," *J. Atmos. Sci.,* vol. 37, pp. 856–867, 1980.
[18] M.-D. Chou, "Atmospheric solar heating rate in the water vapor bands," *J. Climate Appl. Meteor.,* vol. 25, pp. 1532–1542, 1986.
[19] A. A. Lacis and J. E. Hansen, "A parameterization for absorption of solar radiation in the earth's atmosphere," *J. Atmos. Sci.,* vol. 31, pp. 118–133, 1974.
[20] M.-D. Chou, "A solar radiation model for use in climate studies," *J. Atmos. Sci.,* vol. 49, pp. 762–772, 1992.
[21] K. Stamnes, S.-C. Tsay, W. Wiscombe, and K. Jayaweera, "Numerically stable algorithm for discrete-ordinate-method radiative transfer in multiple scattering and emitting layer media," *Appl. Opt.,* vol. 27, pp. 2502–2509, 1988.
[22] J. D. Jackson, *Classical Electrodynamics.* New York: Wiley, 1962.
[23] T. T. Wilheit, "A model for the microwave emissivity of the ocean's surface as a function of wind speed," *IEEE Trans. Geosci. Electron.,* vol. GE-17, pp. 244–249, 1979.
[24] H. J. Liebe, "An updated model for millimeter wave propagation in moist air," *Radio Sci.,* vol. 20, pp. 1069–1089, 1985.
[25] P. W. Barber and S. C. Hill, *Light Scattering by Particles: Computational Methods.* Singapore: World Scientific, 1990.
[26] B. T. Draine and P. J. Flatau, "Discrete dipole approximation for scattering calculations," *J. Opt. Soc. Amer. A,* vol. 11, pp. 1491–1499, 1994.
[27] C. Kummerow, "On the accuracy of the Eddington approximation for radiative transfer in the microwave frequencies," *J. Geophys. Res.,* vol. 98, pp. 2757–2765, 1993.
[28] L. Roberti, J. Haferman, and C. Kummerow, "Microwave radiative transfer through horizontally inhomogeneous precipitating clouds," *J. Geophys. Res.,* vol. 99, pp. 16707–16718, 1994.
[29] W. Robinson, C. Kummerow, and W. S. Olson, "A technique for matching the resolution of microwave measurements from the SSM/I instrument," *IEEE Trans. Geosci. Remote Sensing,* vol. 30, pp. 419–429, 1992.
[30] M. R. Farrar and E. A. Smith, "Spatial resolution enhancement of terrestrial features using deconvolved SSM/I microwave brightness temperatures," *IEEE Trans. Geosci. Remote Sensing,* vol. 30, pp. 349–355, 1992.
[31] A. C. Lorenc, "Analysis methods for numerical weather prediction," *Q. J. R. Meteor. Soc.,* vol. 112, pp. 1177–1194, 1986.
[32] J. R. Eyre, "Inversion of cloudy satellite sounding radiances by nonlinear optimal estimation. I: Theory and simulations for TOVS," *Q. J. R. Meteor. Soc.,* vol. 115, pp. 1001–1026, 1989.
[33] B. Kedem, H. Pavlopoulos, X. Guan, and D. A. Short, "A probability distribution model for rain rate," *J. Appl. Meteor.,* vol. 33, pp. 1486–1493, 1994.
[34] R. F. Adler, H. Y. M. Yeh, N. Prasad, W. K. Tao, and J. Simpson, "Micro-wave simulations of a tropical rainfall system with a three-dimensional cloud model," *J. Appl. Meteor.,* vol. 30, pp. 924–953, 1991.
[35] V. L. Griffin, A. R. Guillory, M. Susko, and J. E. Arnold, "Operations summary for the convection and moisture experiment (CAMEX)," NASA, Tech. Memo., vol. TM-108445, p. 180, 1994.
[36] R. W. Spencer, R. E. Hood, F. J. LaFontaine, E. A. Smith, R. Platt, J. Galliano, V. L. Griffin, and E. Lobl, "High-resolution imaging of rain systems with the advanced microwave precipitation radiometer," *J. Atmos. Ocean. Tech.,* vol. 11, pp. 849–857, 1994.
[37] G. M. Heymsfield, W. Boncyk, S. Bidwell, D. Vandemark, S. Ameen, S. Nicholson, and L. Miller, "Status of the NASA/EDOP airborne radar system," in *26th Conf. Radar Meteor.,* Amer. Meteor. Soc., Norman, OK, 1993, pp. 374–375.
[38] I. J. Caylor, G. M. Heymsfield, S. W. Bidwell, and S. Ameen, "NASA ER-2 Doppler radar calibration for the CAMEX project," NASA, Tech. Memo., vol. 104611, p. 15. (Available from the NASA Center for AeroSpace Information, 800 Elkridge Landing Rd., Linthicum Hts., MD 21090-2934, 1994.)
[39] C. Kummerow and L. Giglio, "A passive microwave technique for estimating rainfall and vertical structure information from space, Part II: Applications to SSM/I data," *J. Appl. Meteor.,* vol. 33, pp. 19–34, 1994.
[40] M. Steiner, R. A. Houze, Jr., and S. E. Yuter, "Climatological characterization of three-dimensional storm structure from operational radar and raingauge data," *J. Appl. Meteor.,* to be published.
[41] E. E. Ebert, "Results from the 3rd Algorithm Intercomparison Project (AIP-3) of the Global Precipitation Climatology Project (GPCP)," Bureau Meteor. Res. Centre, Melbourne, Australia, 1995.
[42] W. S. Olson, C. Kummerow, G. M. Heymsfield, and L. Giglio, "A method for combined passive/active microwave retrievals of cloud and precipitation profiles," *J. Appl. Meteor.,* to be published.
[43] R. H. Johnson, "Partitioning tropical heat and moisture budgets into cumulus and mesoscale components: Implications for cumulus parameterization," *Mon. Wea. Rev.,* vol. 112, pp. 1590–1601, 1984.
[44] W.-K. Tao, J. Simpson, S. Lang, M. McCumber, R. Adler, and R. Penc, "An algorithm to estimate the heating budget from vertical hydrometeor profiles," *J. Appl. Meteor.,* vol. 29, pp. 1232–1244, 1990.
[45] W.-K. Tao, S. Lang, J. Simpson, and R. Adler, "Retrieval algorithms for estimating the vertical profiles of latent heat release: Their applications for TRMM," *J. Meteor. Soc. Japan,* vol. 71, pp. 685–700, 1993.
[46] R. A. Houze, Jr., "Observed structure of mesoscale convective systems and implications for large scale heating," *Q. J. R. Meteor. Soc.,* vol. 115, pp. 425–461, 1989.
[47] K. F. Evans, J. Turk, T. Wong, and G. L. Stephens, "A Bayesian approach to microwave precipitation profile retrieval," *J. Appl. Meteor.,* vol. 34, pp. 260–279, 1995.

Christian Kummerow, photograph and biography not available at the time of publication.

William S. Olson, photograph and biography not available at the time of publication.

Louis Giglio, photograph and biography not available at the time of publication.